22. Lehtimäki KA, Peltola J, Koskikallio E, Keränen T, Honkaniemi J. Expression of cytokines and cytokine receptors in the rat brain after kainic acid-induced seizures. *Brain Res Mol Brain Res.* 2003;110(2):253–260.
23. Oprica M, Spulber SD, Aronsson AF, Post C, Winblad B, Schultzberg M. The influence of kainic acid on core temperature and cytokine levels in the brain. *Cytokine.* 2006;35(1–2):77–87.
24. Eid T, Thomas MJ, Spencer DD, et al. Loss of glutamine synthetase in the human epileptogenic hippocampus: possible mechanism for raised extracellular glutamate in mesial temporal lobe epilepsy. *Lancet.* 2004;363(9402):28–37.
25. Zou J, Wang YX, Mu HJ, et al. Down-regulation of glutamine synthetase enhances migration of rat astrocytes after in vitro injury. *Neurochem Int.* 2011; 58(3):404–413.
26. Hammer J, Alvestad S, Osen KK, Skare Ø, Sonnewald U, Ottersen OP. Expression of glutamine synthetase and glutamate dehydrogenase in the latent phase and chronic phase in the kainate model of temporal lobe epilepsy. *Glia.* 2008; 56(8):856–868.
27. Aronica E, Zurolo E, Iyer A, et al. Upregulation of adenosine kinase in astrocytes in experimental and human temporal lobe epilepsy. *Epilepsia.* 2011;52(9): 1645–1655.
28. Li T, Ren G, Lusardi T, et al. Adenosine kinase is a target for the prediction and prevention of epileptogenesis in mice. *J Clin Invest.* 2008;118(2):571–582.
29. Fedele DE, Gouder N, Güttinger M, et al. Astrogliosis in epilepsy leads to overexpression of adenosine kinase, resulting in seizure aggravation. *Brain.* 2005; 128(pt 10):2383–2395.
30. Pedrazzi M, Patrone M, Passalacqua M, et al. Selective proinflammatory activation of astrocytes by high-mobility group box 1 protein signaling. *J Immunol.* 2007;179(12):8525–8532.
31. Zurolo E, Iyer A, Maroso M, et al. Activation of Toll-like receptor, RAGE and HMGB1 signalling in malformations of cortical development. *Brain.* 2011; 134(pt 4):1015–1032.
32. Viviani B, Bartesaghi S, Gardoni F, et al. Interleukin-1beta enhances NMDA receptor-mediated intracellular calcium increase through activation of the Src family of kinases. *J Neurosci.* 2003;23(25):8692–8700.
33. Hu S, Sheng WS, Ehrlich LC, Peterson PK, Chao CC. Cytokine effects on glutamate uptake by human astrocytes. *Neuroimmunomodulation.* 2000;7(3):153–159.
34. Casamenti F, Prosperi C, Scali C, et al. Interleukin-1beta activates forebrain glial cells and increases nitric oxide production and cortical glutamate and GABA release in vivo: implications for Alzheimer's disease. *Neuroscience.* 1999;91(3): 831–842.
35. Lehtimäki KA, Keränen T, Palmio J, et al. Increased plasma levels of cytokines after seizures in localization-related epilepsy. *Acta Neurol Scand.* 2007;116(4): 226–230.
36. Alapirtti T, Rinta S, Hulkkonen J, Mäkinen R, Keränen T, Peltola J. Interleukin-6, interleukin-1 receptor antagonist and interleukin-1beta production in patients with focal epilepsy: a video-EEG study. *J Neurol Sci.* 2009;280(1–2):94–97.

PET Imaging Analysis with ^{64}Cu in Disulfiram Treatment for Aberrant Copper Biodistribution in Menkes Disease Mouse Model

Shiho Nomura[1], Satoshi Nozaki[2], Takashi Hamazaki[1], Taisuke Takeda[1], Eiichi Ninomiya[1], Satoshi Kudo[1], Emi Hayashinaka[2], Yasuhiro Wada[2], Tomoko Hiroki[3], Chie Fujisawa[3], Hiroko Kodama[3], Haruo Shintaku[1], and Yasuyoshi Watanabe[2]

[1]Department of Pediatrics, Graduate School of Medicine, Osaka City University, Osaka, Japan; [2]RIKEN Center for Life Science Technologies, Kobe, Japan; and [3]Department of Pediatrics, School of Medicine, Teikyo University, Tokyo, Japan

Menkes disease (MD), an X-linked recessive disorder of copper metabolism caused by mutations in the copper-transporting ATP7A gene, results in growth failure and severe neurodegeneration in early childhood. Subcutaneous copper-histidine injection is the standard treatment for MD, but it has limited clinical efficacy. Furthermore, long-term copper injection causes excess copper accumulation in the kidneys, resulting in renal dysfunction. To attempt to resolve this issue, we used PET imaging with ^{64}Cu to investigate the effects of disulfiram on copper biodistribution in living mice serving as an animal model for MD (MD model mice). **Methods:** Macular mice were used as MD model mice, and C3H/He mice were used as wild-type mice. Mice were pretreated with 2 types of chelators (disulfiram, a lipophilic chelator, and D-penicillamine, a hydrophilic chelator) 30 min before $^{64}CuCl_2$ injection. After $^{64}CuCl_2$ injection, emission scans covering the whole body were performed for 4 h. After the PET scans, the brain and kidneys were analyzed for radioactivity with γ counting and autoradiography. **Results:** After copper injection alone, marked accumulation of radioactivity (^{64}Cu) in the liver was demonstrated in wild-type mice, whereas in MD model mice, copper was preferentially accumulated in the kidneys (25.56 ± 3.01 percentage injected dose per gram [%ID/g]) and was detected to a lesser extent in the liver (13.83 ± 0.26 %ID/g) and brain (0.96 ± 0.08 %ID/g). Copper injection with disulfiram reduced excess copper accumulation in the kidneys (14.54 ± 2.68 %ID/g) and increased copper transport into the liver (29.42 ± 0.98 %ID/g) and brain (5.12 ± 0.95 %ID/g) of MD model mice. Copper injection with D-penicillamine enhanced urinary copper excretion and reduced copper accumulation in most organs in both mouse groups. Autoradiography demonstrated that disulfiram pretreatment induced copper transport into the brain parenchyma and reduced copper accumulation in the renal medulla. **Conclusion:** PET studies with ^{64}Cu revealed that disulfiram had significant effects on the copper biodistribution of MD. Disulfiram increased copper transport into the brain and reduced copper uptake in the kidneys of MD model mice. The application of ^{64}Cu PET for the treatment of MD and other copper-related disorders may be useful in clinical settings.

Received Aug. 30, 2013; revision accepted Jan. 1, 2014.
For correspondence or reprints contact: Yasuyoshi Watanabe, RIKEN Center for Life Science Technologies, 6-7-3 Minatojima-minamimachi, Chuo-ku, Kobe, Hyogo 650-0047, Japan.
E-mail: yywata@riken.jp
Published online Mar. 13, 2014.

Key Words: Menkes disease; copper; PET; disulfiram; D-penicillamine

J Nucl Med 2014; 55:845–851
DOI: 10.2967/jnumed.113.131797

Menkes disease (MD) is an inherited X-linked disorder of copper metabolism caused by mutations in the *ATP7A* gene, which encodes a copper-transporting protein (*1,2*). ATP7A controls copper transport from the cytosol to the Golgi apparatus and copper excretion from cells (*3*). In patients with MD, dysfunctional ATP7A causes a failure of copper absorption from the intestine (*4*). Because macular mice possess a mutation in the mottled gene (*atp7a*) and have a clinical phenotype and biochemical abnormalities similar to those of MD patients, they can serve as an animal model for MD (i.e., MD model mice) (*5–7*). Systemic copper deficiency was demonstrated to cause dysfunction of copper-dependent enzymes and to result in multisystem disorders, such as severe neurodegeneration, connective tissue abnormalities, and kinky hair, in these mice (*8,9*).

To correct systemic copper deficiencies in MD, subcutaneous copper-histidine injection is the standard treatment (*10–12*), but its efficacy depends on the age-related maturation of the blood–brain barrier (BBB) or residual copper transport by a partially functional gene (*12–14*). When copper treatment is initiated in the neonatal period or early infancy, when the BBB is immature, the injected copper is delivered to the neurons and, thus, is an effective treatment for neurologic disorders (*11,14*). However, parenteral copper administration has limited clinical efficacy in MD patients more than 2 mo old because the injected copper is trapped in the maturing BBB (*11*).

Another important aspect of parenteral copper administration is that copper treatment is sometimes associated with excess copper accumulation in the kidneys, leading to renal dysfunction in patients and macular mice with MD (*6,15*). Previous reports demonstrated that copper administration lengthened the life-span of MD model mice but that copper accumulation to toxic levels in the kidneys led to severe renal damage (*16,17*). The mechanisms of copper-induced renal damage have not been fully elucidated; however, the oxidative potential of copper is considered to induce free-radical production and to result in cellular damage (*18,19*). To date, there have been no studies on the development of a treatment focusing on the prevention of copper accumulation in the kidneys.

Several attempts have been made to develop novel methods to address insufficient copper transport into the brain in the presence of a maturing BBB. Kodama et al. (*20*) and Munakata et al. (*21*) demonstrated that the use of a combination of copper and disulfiram, a lipophilic chelator, improved copper deficiency in the brain of MD model mice (macular mice). Administered disulfiram is immediately converted into sodium diethyldithiocarbamate (DEDTC) by glutathione reductase, and the complex of copper and DEDTC can pass through the BBB (*22–24*). To advance these findings to clinical application, it is important to elucidate the time course of copper biodistribution with and without disulfiram. Therefore, an evaluation of disulfiram via pharmacology safety studies, such as absorption, distribution, metabolism, and excretion studies, must be performed in an animal model before clinical trials in humans. Traditionally, the evaluation of absorption, distribution, metabolism, and excretion in the development of pharmaceuticals has involved autoradiography of the whole body and the detection of radioactivity associated with dissected tissues by use of radioactive ^{125}I- or ^{111}In-labeled pharmaceuticals (*25*). However, recently developed molecular imaging technologies allow the visualization and quantitative measurement of biologic processes in living systems (*26–28*). Radioisotope-based molecular imaging techniques, such as PET, have been used for the noninvasive detection of pharmacodynamics in the gut and for the determination of functional changes in the nervous system (*26,27*).

In this study, we aimed to investigate the effects of 2 types of copper chelators (disulfiram, a lipophilic chelator, and D-penicillamine, a hydrophilic chelator) on copper biodistribution after copper injection in MD model mice by PET imaging with ^{64}Cu.

MATERIALS AND METHODS

Animals and Disulfiram and D-Penicillamine Pretreatments

This study was performed in accordance with international standards for animal welfare and institutional guidelines and was approved by the animal care and use committees of Osaka City University, Osaka, Japan, and RIKEN Center for Life Science Technologies, Kobe, Japan. We used 4- to 7-wk-old C3H/He mice (body weight, 16–24 g) purchased from Japan SLC as wild-type mice and 4- to 8-wk-old macular mice (7–22 g) bred at Teikyo University as MD model mice (*5–7*).

Mice were anesthetized with a mixture of 1.5% isoflurane (Abbott), nitrous oxide (0.5 L/min), and 100% oxygen (1.5 L/min). In mice pretreated with disulfiram (100 mg/kg; Wako Pure Chemicals), disulfiram diluted with sesame oil was injected intraperitoneally. In mice pretreated with D-penicillamine (100 mg/kg; Wako Pure Chemicals), D-penicillamine diluted with saline was injected subcutaneously.

$^{64}CuCl_2$ PET

$^{64}CuCl_2$was produced from the cyclotron at the RIKEN Center for Life Science Technologies. At 30 min after disulfiram or D-penicillamine pretreatment, $^{64}CuCl_2$ corresponding to an activity of 30 MBq was administered via the tail vein. Mice were imaged in the prone position in a small-animal PET scanner (microPET Focus220; Siemens Medical Solutions Inc.). Continuous PET scanning was performed for 4 h immediately after $^{64}CuCl_2$ injection. PET data were acquired in the list mode and reconstructed by use of a filtered backprojection algorithm with a ramp filter cutoff at the Nyquist frequency, attenuation correction, and no scatter correction. The PET image data were displayed and analyzed with IDL VM 6.3 (Exelis Inc.) and ASIPro VM (Siemens Medical Solutions Inc.) software. Regions of interest were drawn manually on PET images, and the percentage injected dose per gram of tissue (%ID/g) was calculated with the software. Three mice were scanned for each experimental group, and data from these mice were subjected to statistical analysis.

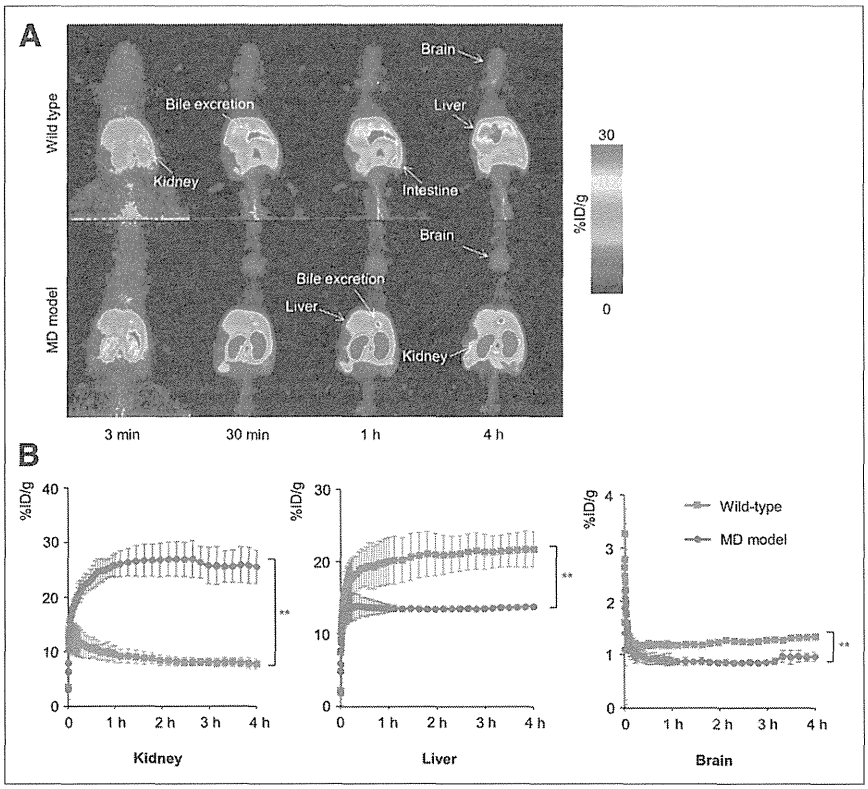

FIGURE 1. PET image analysis after $^{64}CuCl_2$ injection in wild-type and MD model mice. (A) Coronal section of whole-body PET image 4 h after $^{64}CuCl_2$ injection in MD model mice. (B) Time–activity curve for kidneys, liver, and brain 4 h after $^{64}CuCl_2$ injection. MD model mice showed higher level of copper accumulation in kidneys and lower levels of copper accumulation in liver and brain than wild-type mice. $^{**}P < 0.01$.

γ Counting and Ex Vivo Autoradiography

^{64}Cu accumulation was evaluated by γ counting at 4 h after $^{64}CuCl_2$ injection as described previously (*29*). Each sample was counted in a 1470 WIZARD automatic γ counter (Wallac). Tissues were weighed, and the amount of radioactivity was calculated as the %ID/g. Six wild-type mice and 4 MD model mice were included in each experimental group, and data from these mice were subjected to statistical analysis.

For the quantification of emission data, ex vivo brain and renal autoradiography was performed as described previously (*26*). Brain tissue was sliced into coronal sections and kidney tissue was sliced into sagittal sections (1 mm thick) with a brain matrix (RBM-2000C; ASI instruments Inc.). Brain and kidney slices were placed on an imaging plate (BAS-SR2040; Fuji Photo Film) for 15 and 5 min, respectively. Exposed imaging plates

were scanned with an imaging analyzer (FLA-7000; Fuji). Reproducibility was confirmed in 3 independent experiments.

Statistical Analyses

All data are presented as mean ± SD. Statistical analyses were performed with commercially available software (JMP version 9; SAS Institute). Statistical analyses of PET data with time–activity curves were performed with repeated-measures ANOVA. Statistical analyses of γ-counting data were performed with the Wilcoxon test.

RESULTS

Copper Accumulation without Chelator in Wild-Type and MD Model Mice

In wild-type mice, copper uptake in the kidneys was confirmed soon after copper injection, reached a maximum level, and gradually decreased (7.74 ± 0.90 %ID/g at 4 h). Copper excretion into bile could be seen, and we detected copper uptake in the intestine. The marked copper uptake in the liver continued to increase during PET imaging (21.80 ± 2.42 %ID/g at 4 h). In the brain, copper uptake was low but increased gradually during PET imaging (1.34 ± 0.03 %ID/g at 4 h) (Fig. 1).

In MD model mice, copper uptake in the kidneys was markedly elevated (25.56 ± 3.01 %ID/g at 4 h) and was 4-fold higher than that in wild-type mice ($P < 0.01$). Copper excretion into bile was evident, and copper uptake in the liver was maintained at a plateau (13.83 ± 0.26 %ID/g at 4 h). Copper uptake in the brain was lower (0.96 ± 0.08 %ID/g at 4 h) than that in the kidneys and liver and was significantly lower than that in wild-type mice ($P < 0.01$) (Fig. 1).

The γ-counting data supported the PET scan data showing that copper uptake in the kidneys of MD model mice was significantly higher than that in wild-type mice (14.47 ± 3.39 %ID/g in wild-type mice and 84.38 ± 12.39 %ID/g in MD model mice; $n = 4–6$; $P < 0.05$). On the other hand, copper uptake in the liver of MD model mice was significantly lower than that in wild-type mice (38.80 ± 3.46 %ID/g in wild-type mice and 22.27 ± 1.93 %ID/g in MD model mice; $n = 4–6$; $P < 0.05$). Copper uptake in the brain in both wild-type and MD model mice was low, with no significant differences (Table 1).

These data confirmed that systemic copper injection without chelator resulted in marked copper accumulation in the kidneys of MD model mice. The uptake of injected copper in the liver and brain of MD model mice was lower than that in wild-type mice.

Effects of Disulfiram or D-Penicillamine Pretreatment in Wild-Type Mice

There were no significant differences in copper uptake in the kidneys of mice pretreated with disulfiram and mice not pretreated with the chelator. In the liver, disulfiram pretreatment increased copper uptake (28.82 ± 7.62 %ID/g at 4 h). In the brain, copper uptake was gradually elevated during PET imaging (5.32 ± 0.03 %ID/g at 4 h), and there were significant differences between mice receiving and mice not receiving disulfiram pretreatment ($P < 0.01$) (Fig. 2). On the other hand, D-penicillamine pretreatment significantly reduced copper uptake in the kidneys compared with that in mice not pretreated with the chelator ($P < 0.01$). Copper uptake in the liver and brain at 4 h was markedly lower in mice pretreated with D-penicillamine (6.80 ± 1.22 %ID/g in the liver and 0.40 ± 0.08 %ID/g in the brain) than in those not pretreated with the chelator ($P < 0.01$) (Figs. 2A and 2C).

The γ-counting data confirmed that disulfiram pretreatment increased copper accumulation in the brain, heart, liver, spleen, muscle, and blood and decreased it in the stomach, intestine, and kidneys of wild-type mice. D-Penicillamine enhanced urinary copper excretion and decreased copper accumulation in all organs investigated (Table 1).

These data confirmed that disulfiram increased copper accumulation in the brain and liver but did not alter copper accumulation in the kidneys of wild-type mice. D-Penicillamine strongly enhanced urinary copper excretion in wild-type mice.

Effects of Disulfiram or D-Penicillamine Pretreatment in MD Model Mice

Copper accumulation in the kidneys of MD model mice at 4 h was significantly lower in mice pretreated with disulfiram or

TABLE 1
γ-counting Data for Each Organ 4 Hours After $^{64}CuCl_2$ Injection

	Mean ± SD %ID/g for:					
	Wild-type mice			MD model mice		
Organ	No chelator ($n = 6$)	Disulfiram ($n = 6$)	D-Penicillamine ($n = 6$)	No chelator ($n = 4$)	Disulfiram ($n = 4$)	D-Penicillamine ($n = 4$)
Brain	1.00 ± 0.17	7.89 ± 1.08*	0.34 ± 0.05*	1.21 ± 0.19	4.73 ± 2.74*	0.44 ± 0.16*
Heart	6.87 ± 1.50	12.99 ± 6.06*	2.06 ± 0.28*	2.17 ± 0.18†	10.36 ± 5.19‡	2.09 ± 1.48
Lungs	19.39 ± 5.02	16.36 ± 2.15	5.28 ± 2.25*	8.86 ± 1.35†	11.62 ± 4.77	2.38 ± 0.55‡
Liver	38.80 ± 3.46	61.61 ± 13.51‡	14.04 ± 2.96*	22.27 ± 1.93†	31.11 ± 15.06	16.04 ± 2.96‡
Pancreas	6.28 ± 1.42	8.75 ± 3.00	2.73 ± 0.66*	2.33 ± 1.15†	5.14 ± 2.83	1.56 ± 0.81
Spleen	5.28 ± 1.13	8.91 ± 2.40*	1.62 ± 0.56*	4.03 ± 0.17	5.66 ± 2.37	2.65 ± 1.15
Stomach	30.01 ± 12.81	6.45 ± 1.33*	11.89 ± 1.89*	29.61 ± 6.63	5.91 ± 3.58*	9.25 ± 2.82*
Intestine	18.02 ± 3.45	6.17 ± 1.29*	6.83 ± 1.15*	21.89 ± 2.12	4.67 ± 1.72‡	8.71 ± 2.93‡
Kidneys	14.47 ± 3.39	15.31 ± 2.34	9.76 ± 1.32‡	84.38 ± 12.39†	22.46 ± 9.64‡	45.46 ± 17.54
Muscle	0.81 ± 0.24	2.18 ± 1.03*	0.47 ± 0.35	0.59 ± 0.05	1.34 ± 0.98	0.33 ± 0.29
Blood	3.01 ± 0.74	6.04 ± 1.02*	1.15 ± 0.40*	1.64 ± 0.27†	1.50 ± 0.17	1.11 ± 0.10‡
Urine	5.04 ± 3.05	0.34 ± 0.12*	199.24 ± 123.42*	4.75 ± 0.96	0.40 ± 0.44‡	384.62 ± 380.52‡

*$P < 0.01$ for no chelator vs. disulfiram or D-penicillamine in wild-type or MD model mice.
†$P < 0.05$ for no chelator in wild-type mice vs. no chelator in MD model mice.
‡$P < 0.05$ for no chelator vs. disulfiram or D-penicillamine in wild-type or MD model mice.

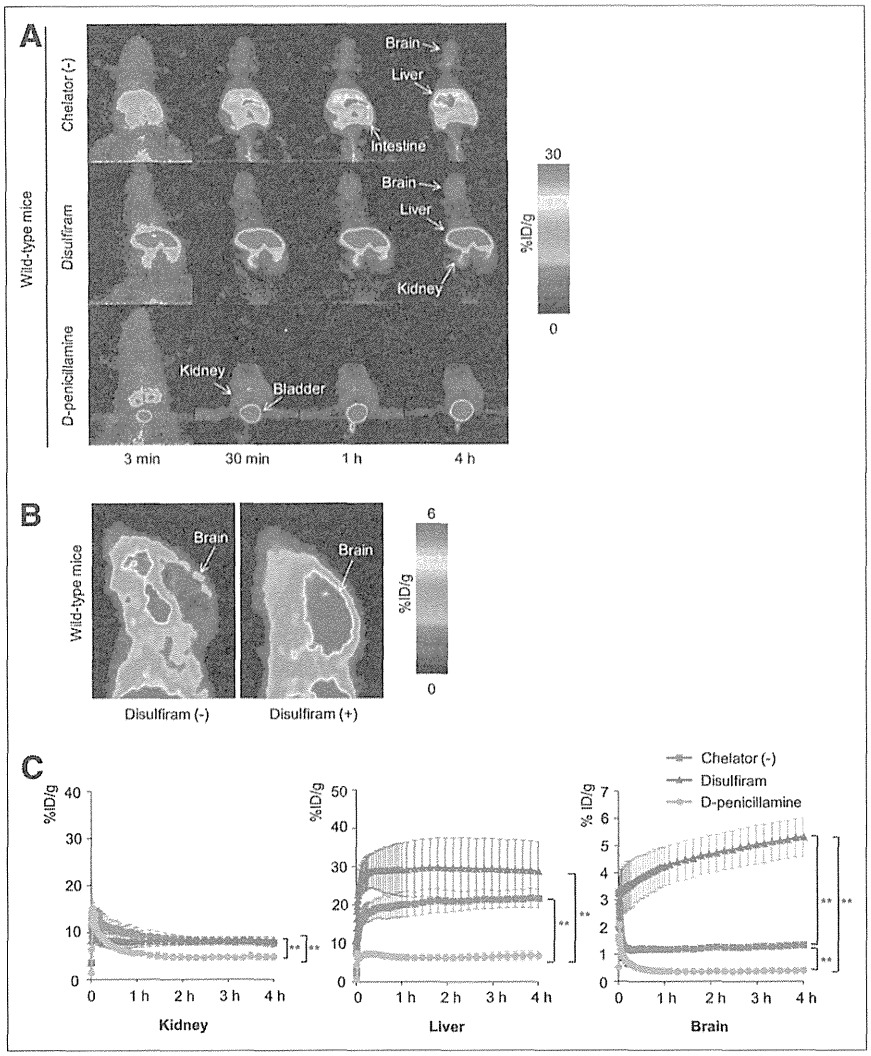

FIGURE 2. PET image analysis after $^{64}CuCl_2$ injection and disulfiram or D-penicillamine pretreatment in wild-type mice. (A) Coronal section of whole-body PET image 4 h after $^{64}CuCl_2$ injection in wild-type mice. Chelator (−) = no chelator. (B) Sagittal section of brain PET image 4 h after $^{64}CuCl_2$ injection. (C) Time–activity curve for kidneys, liver, and brain 4 h after $^{64}CuCl_2$ injection. In wild-type mice, disulfiram increased copper accumulation in liver and brain, and D-penicillamine enhanced urinary copper excretion and decreased copper accumulation in all organs. Data are mean ± SD. $^{**}P < 0.01$.

D-penicillamine than in mice not pretreated with a chelator (14.54 ± 2.68 %ID/g in mice pretreated with disulfiram and 16.71 ± 2.89 %ID/g in mice pretreated with D-penicillamine) ($P < 0.05$). On the other hand, disulfiram pretreatment significantly increased copper accumulation in the liver (29.42 ± 0.98 %ID/g) and brain (5.12 ± 0.95 %ID/g) at 4 h compared with that in mice not pretreated with the chelator ($P < 0.01$). D-Penicillamine pretreatment decreased copper accumulation in the brain and liver ($P < 0.01$) (Fig. 3).

The γ-counting data confirmed that disulfiram pretreatment increased copper accumulation in the brain and heart and decreased it in the stomach, intestine, and kidneys of MD model mice. D-Penicillamine enhanced urinary copper excretion and decreased copper accumulation in most organs investigated (Table 1).

These data confirmed that disulfiram increased copper accumulation in the brain and liver and decreased copper accumulation in the kidneys of MD model mice. D-Penicillamine strongly enhanced urinary copper excretion and decreased copper accumulation in the kidneys, brain, and liver of MD model mice.

Brain Autoradiography

At 4 h after copper administration without a chelator, high levels of copper accumulation were observed in the lateral ventricle and the third ventricle in wild-type mice. MD model mice showed a similar pattern of copper accumulation, but the overall level of copper accumulation was lower than that in wild-type mice. Disulfiram pretreatment markedly increased copper uptake in the brain parenchyma in both wild-type and MD model mice. High levels of copper uptake were observed in the cerebral cortex and thalamus, whereas copper uptake in the ventricles was not prominent (Fig. 4A).

Renal Autoradiography

Compared with wild-type mice, MD model mice showed marked accumulation of injected copper in the renal tissue and notable accumulation in both the cortex and the medulla. Both chelators (disulfiram and D-penicillamine) decreased copper uptake in the renal tissue of MD model mice, but the copper distribution patterns in the disulfiram and D-penicillamine pretreatment groups were different. Disulfiram decreased copper uptake in the medulla, whereas D-penicillamine decreased it in the cortex (Fig. 4B).

DISCUSSION

PET is a functional imaging technique with high sensitivity. With the development of dedicated small-animal PET scanners, it is possible to perform functional imaging in small animals at high spatial resolutions (*26–28*). Using a small-animal PET imaging system, we obtained the first evidence—to our knowledge—that disulfiram pretreatment efficiently corrects inappropriate copper biodistribution in living MD model mice. The dynamics of administered copper and the time course of the effects of disulfiram in living animals strengthen the results of previous studies demonstrating the effects of disulfiram with conventional methods, such as histochemistry in postmortem animals (*20,23*). These data accelerate our goal—the clinical application of disulfiram treatment in MD patients.

For macular mice, well-established as an MD model, the present study confirmed that copper accumulation after systemic copper injection without a chelator shifted to the kidneys rather than the liver and brain, as in wild-type mice; these findings are consistent with previous findings for MD patients and MD model mice (*2,12*). Copper deficiency in the brain due to copper transport dysfunction at the BBB causes severe neurodegeneration in MD (*8*); therefore, it is important to develop an effective strategy for improving copper transport into the brain on the basis of copper

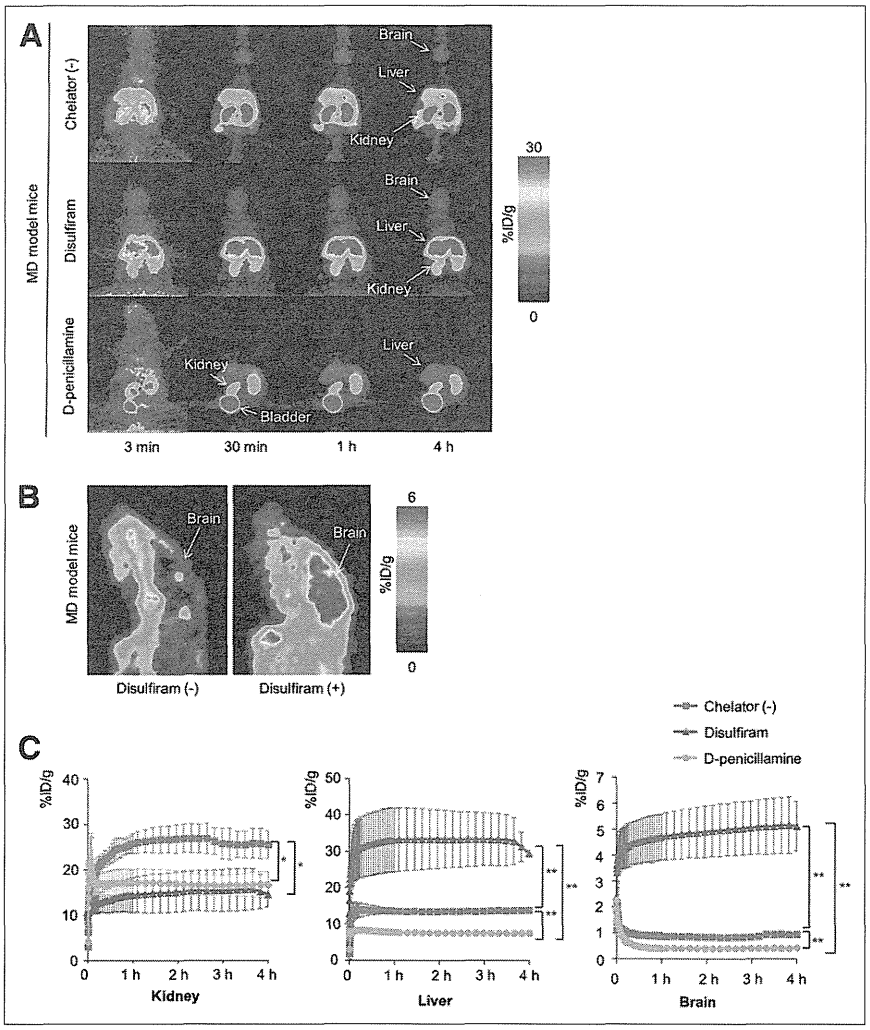

FIGURE 3. PET image analysis after $^{64}CuCl_2$ injection and disulfiram or D-penicillamine pretreatment in MD model mice. (A) Coronal section of whole-body PET image 4 h after $^{64}CuCl_2$ injection. Chelator (−) = no chelator. (B) Sagittal section of brain PET image 4 h after $^{64}CuCl_2$ injection. (C) Time–activity curve for kidneys, liver, and brain 4 h after $^{64}CuCl_2$ injection. In MD model mice, disulfiram decreased copper accumulation in kidneys and increased copper accumulation in liver and brain, and D-penicillamine enhanced urinary copper excretion and decreased copper accumulation in all organs. Data are mean ± SD. $^*P < 0.05$. $^{**}P < 0.01$.

dynamics in living systems. PET imaging provided direct visual evidence that disulfiram rapidly increased copper uptake in the brain of MD model mice on the basis of copper dynamics, including the detailed time course of copper transport in the whole body of a living mouse. Our quantitative time–activity curve analysis was sensitive enough to detect defective copper uptake in the brain parenchyma of MD model mice, which could not be evaluated by conventional γ counting because of high background activity from the periventricular vasculature (Figs. 1B and 4A; Table 1). The effectiveness of disulfiram pretreatment and details about copper dynamics would contribute to accelerating human clinical trials of disulfiram therapy for MD patients. On the other hand, excess copper transport may pose a risk for free-radical production, resulting in cellular damage (*18*). Further study is needed to determine how to modulate copper transport to the brain to normalize neurologic function in MD patients with various background factors, such as age and gene mutation type. PET imaging is effective for evaluating safe doses of copper or disulfiram for the maintenance of appropriate copper accumulation in the brain in living MD mice and humans.

With regard to the mechanisms responsible for the effects of disulfiram on copper transport into the brain, the hydrophobicity of DEDTC—an active and converted form of disulfiram—is known to allow the complex of DEDTC and copper to permeate cellular membranes, including the Golgi apparatus (*20,23,30*). However, the formation of the complex was not demonstrated in vivo in those studies. An alternative mechanism of copper transport (e.g., Ctr1) could not be ruled out as an explanation for the effects of disulfiram on copper transport. Our ex vivo brain autoradiography findings clearly demonstrated that the copper injected with disulfiram passed through the BBB and was taken up into the brain parenchyma. Interestingly, we found that copper uptake was most prominent in the thalamus and then in the cerebellar cortex. As for the regional differences in copper biodistribution, Szerdahelyi and Kása (*22*) demonstrated that the effects of a lipophilic chelator depended on the brain region, with the highest increase being observed in the hippocampus. Their histochemistry study also revealed increased accumulation of copper in the glia and neurons. The bioavailability of chelator-bound copper is crucial for clinical application. A recent study demonstrated that disulfiram treatment increased cuproenzyme (cytochrome *c* oxidase) activity in the brain, and the authors suggested that the transported copper was indeed bioavailable after disulfiram treatment (*30*). On the basis of the findings of present and previous studies, detailed data for copper biodistribution in the brain remain controversial; therefore, further evidence of copper biodistribution in the brain should be gathered with PET imaging and other basic technologies.

Another important aspect of the present study was the significant disulfiram-mediated reduction of copper accumulation in the kidneys of MD model mice. Long-term copper injection has a risk of causing copper accumulation to toxic levels in the kidneys, leading to severe renal damage (*15–17*). The present study confirmed that, without disulfiram pretreatment, systemically administered copper was preferentially taken up by the kidneys of living MD model mice. PET imaging analysis confirmed that disulfiram pretreatment markedly improved aberrant copper accumulation in the kidneys, thus reducing the risk of renal complications associated with long-term copper treatment. A previous study demonstrated the efficacy of disulfiram treatment in mice but revealed excess copper accumulation in the kidneys (*30*). Differences in the dose and route of administration of copper and disulfiram, the timing of disulfiram administration, and the age of the animals tested may be responsible for the inconsistent

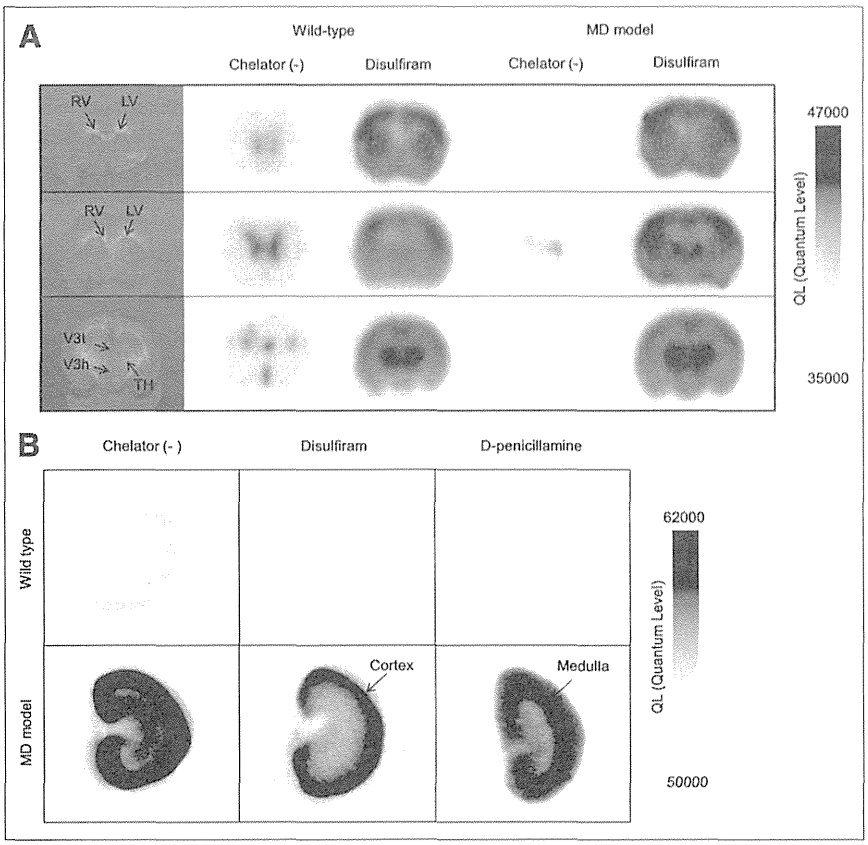

FIGURE 4. Autoradiography results. (A) Brain autoradiography after $^{64}CuCl_2$ injection. Disulfiram pretreatment increased uptake of $^{64}CuCl_2$ in cortex and thalamus. Chelator (−) = no chelator; LV = left ventricle; RV = right ventricle; TH = thalamus; V3h = hypothalamic part of third ventricle; V3t = thalamic part of third ventricle. (B) Renal autoradiography 4 h after $^{64}CuCl_2$ injection (sagittal sections). Disulfiram decreased copper accumulation in medulla, and D-penicillamine decreased copper accumulation in cortex.

results of the present study and previous studies. Because copper is usually administered subcutaneously in clinical settings, it is important to compare biodistributions achieved with various routes of administration (*31*). Further study is needed to establish effective and safe treatment with disulfiram and the PET imaging system in living animals.

In MD patients, primary renal dysfunction is caused by copper accumulation mainly in the medulla (renal tubule) (*15*); therefore, the finding that disulfiram was able to reduce copper uptake in the medulla was significant. Our ex vivo autoradiography analysis of the kidneys with 2 types of chelators revealed different copper distribution patterns in renal tissue: disulfiram-mediated reduction of copper uptake in the medulla and D-penicillamine–mediated reduction of copper uptake in the cortex. These observations further suggest the efficacy of the use of the combination of copper and disulfiram in MD patients.

CONCLUSION

The present PET imaging study clarified that disulfiram pretreatment provided 2 favorable outcomes for copper replacement therapy in MD model mice: increased copper uptake in the brain and reduced copper uptake in the kidneys. Our findings strongly suggest that copper-chelating agents can act as nonenzymatic transporters of copper to correct the biodistribution of copper in MD patients. Noninvasive PET imaging is useful for visualizing and quantifying copper dynamics, accelerating the clinical application of copper chelators for MD.

DISCLOSURE

The costs of publication of this article were defrayed in part by the payment of page charges. Therefore, and solely to indicate this fact, this article is hereby marked "advertisement" in accordance with 18 USC section 1734. This study was supported by a grant for research on intractable diseases from MHLW of Japan (H23-nannchi-ippann-091) and JSPS KAKENHI grant 24591523. No other potential conflict of interest relevant to this article was reported.

ACKNOWLEDGMENTS

We thank Daisuke Tokuhara, MD, PhD, and Hiroki Fujioka, MD, PhD, for their efforts.

REFERENCES

1. Vulpe C, Levinson B, Whitney S, Packman S, Gitschier J. Isolation of a candidate gene for Menkes disease and evidence that it encodes a copper-transporting ATPase. *Nat Genet.* 1993;3:7–13.
2. Kodama H, Murata Y. Molecular genetics and pathophysiology of Menkes disease. *Pediatr Int.* 1999;41:430–435.
3. Lutsenko S, Barnes NL, Bartee MY, Dmitriev OY. Function and regulation of human copper-transporting ATPases. *Physiol Rev.* 2007;87:1011–1046.
4. Kodama H, Abe T, Takama M, Takahashi I, Kodama M, Nishimura M. Histochemical localization of copper in the intestine and kidney of macular mice: light and electron microscopic study. *J Histochem Cytochem.* 1993;41:1529–1535.
5. Kodama H, Meguro Y, Abe T, et al. Genetic expression of Menkes disease in cultured astrocytes of the macular mouse. *J Inherit Metab Dis.* 1991;14:896–901.
6. Shiraishi N, Aono K, Taguchi T. Copper metabolism in the macular mutant mouse: an animal model of Menkes's kinky-hair disease. *Biol Neonate.* 1988;54:173–180.
7. Murata Y, Kodama H, Abe T, et al. Mutation analysis and expression of the mottled gene in the macular mouse model of Menkes disease. *Pediatr Res.* 1997;42:436–442.
8. Kodama H, Murata Y, Kobayashi M. Clinical manifestations and treatment of Menkes disease and its variants. *Pediatr Int.* 1999;41:423–429.
9. Meguro Y, Kodama H, Abe T, Kobayashi S, Kodama Y, Nishimura M. Changes of copper level and cytochrome *c* oxidase activity in the macular mouse with age. *Brain Dev.* 1991;13:184–186.
10. Kreuder J, Otten A, Fuder H, et al. Clinical and biochemical consequences of copper-histidine therapy in Menkes disease. *Eur J Pediatr.* 1993;152:828–832.
11. Sarkar B, Lingertat-Walsh K, Clarke JT. Copper-histidine therapy for Menkes disease. *J Pediatr.* 1993;123:828–830.
12. Wenk G, Suzuki K. The effect of copper supplementation on the concentration of copper in the brain of the brindled mouse. *Biochem J.* 1982;205:485–487.
13. Kaler SG, Das S, Levinson B, et al. Successful early copper therapy in Menkes disease associated with a mutant transcript containing a small in-frame deletion. *Biochem Mol Med.* 1996;57:37–46.
14. Christodoulou J, Danks DM, Sarkar B, et al. Early treatment of Menkes disease with parenteral copper-histidine: long-term follow-up of four treated patients. *Am J Med Genet.* 1998;76:154–164.
15. Kodama H, Okabe I, Kihara A, Mori Y, Okaniwa M. Renal tubular function of patients with classical Menkes disease. *J Inherit Metab Dis.* 1992;15:157–158.

16. Lenartowicz M, Kowal M, Buda-Lewandowska D, Styrna J. Pathological structure of the kidney from adult mice with mosaic mutation. *J Inherit Metab Dis.* 2002;25:647–659.
17. Lenartowicz M, Windak R, Tylko G, Kowal M, Styrna J. Effects of copper supplementation on the structure and content of elements in kidneys of mosaic mutant mice. *Biol Trace Elem Res.* 2010;136:204–220.
18. Cai L, Li XK, Song Y, Cherian MG. Essentiality, toxicology and chelation therapy of zinc and copper. *Curr Med Chem.* 2005;12:2753–2763.
19. Lutsenko S, Petris MJ. Function and regulation of the mammalian copper-transporting ATPases: insights from biochemical and cell biological approaches. *J Membr Biol.* 2003;191:1–12.
20. Kodama H, Sato E, Gu YH, Shiga K, Fujisawa C, Kozuma T. Effect of copper and diethyldithiocarbamate combination therapy on the macular mouse, an animal model of Menkes disease. *J Inherit Metab Dis.* 2005;28:971–978.
21. Munakata M, Kodama H, Fujisawa C, et al. Copper-trafficking efficacy of copper-pyruvaldehyde bis(N_4-methylthiosemicarbazone) on the macular mouse, an animal model of Menkes disease. *Pediatr Res.* 2012;72:270–276.
22. Szerdahelyi P, Kása P. Regional differences in the uptake of exogenous copper into rat brain after acute treatment with sodium diethyldithiocarbamate: a histochemical and atomic absorption spectrophotometric study. *Histochemistry.* 1987;86:627–632.
23. Aaseth J, Søli NE, Førre O. Increased brain uptake of copper and zinc in mice caused by diethyldithiocarbamate. *Acta Pharmacol Toxicol (Copenh).* 1979;45:41–44.
24. Johansson B, Stankiewicz Z. Bis-(diethyldithiocarbamato) copper complex: a new metabolite of disulfiram? *Biochem Pharmacol.* 1985;34:2989–2991.
25. Staud F, Nishikawa M, Morimoto K, Takakura Y, Hashida M. Disposition of radioactivity after injection of liver-targeted proteins labeled with ^{111}In or ^{125}I: effect of labeling on distribution and excretion of radioactivity in rats. *J Pharm Sci.* 1999;88:577–585.
26. Mizuma H, Shukuri M, Hayashi T, Watanabe Y, Onoe H. Establishment of in vivo brain imaging method in conscious mice. *J Nucl Med.* 2010;51:1068–1075.
27. Yamashita S, Takashima T, Kataoka M, et al. PET imaging of the gastrointestinal absorption of orally administered drugs in conscious and anesthetized rats. *J Nucl Med.* 2011;52:249–256.
28. Takashima T, Wu C, Takashima-Hirano M, et al. Evaluation of breast cancer resistance protein function in hepatobiliary and renal excretion using PET with ^{11}C-SC-62807. *J Nucl Med.* 2013;54:267–276.
29. Yamato M, Kataoka Y, Mizuma H, Wada Y, Watanabe Y. PET and macro- and microautoradiographic studies combined with immunohistochemistry for monitoring rat intestinal ulceration and healing processes. *J Nucl Med.* 2009;50:266–273.
30. Bhadhprasit W, Kodama H, Fujisawa C, Hiroki T, Ogawa E. Effect of copper and disulfiram combination therapy on the macular mouse, a model of Menkes disease. *J Trace Elem Med Biol.* 2012;26:105–108.
31. Martin SM, O'Donnell RT, Kukis DL, et al. Imaging and pharmacokinetics of ^{64}Cu-DOTA-HB22.7 administered by intravenous, intraperitoneal, or subcutaneous injection to mice bearing non-Hodgkin's lymphoma xenografts. *Mol Imaging Biol.* 2009;11:79–87.

JNM The Journal of NUCLEAR MEDICINE

PET Imaging Analysis with ^{64}Cu in Disulfiram Treatment for Aberrant Copper Biodistribution in Menkes Disease Mouse Model

Shiho Nomura, Satoshi Nozaki, Takashi Hamazaki, Taisuke Takeda, Eiichi Ninomiya, Satoshi Kudo, Emi Hayashinaka, Yasuhiro Wada, Tomoko Hiroki, Chie Fujisawa, Hiroko Kodama, Haruo Shintaku and Yasuyoshi Watanabe

J Nucl Med. 2014;55:845-851.
Published online: March 13, 2014.
Doi: 10.2967/jnumed.113.131797

The Journal of Nuclear Medicine is published monthly.
SNMMI | Society of Nuclear Medicine and Molecular Imaging
1850 Samuel Morse Drive, Reston, VA 20190.
(Print ISSN: 0161-5505, Online ISSN: 2159-662X)

SNMMI SOCIETY OF NUCLEAR MEDICINE AND MOLECULAR IMAGING

nature publishing group

Role of per-rectal portal scintigraphy in long-term follow-up of congenital portosystemic shunt

Yuki Cho[1], Daisuke Tokuhara[1], Taro Shimono[2], Akira Yamamoto[2], Shigeaki Higashiyama[3], Kohei Kotani[3], Joji Kawabe[3], Yoshiyuki Okano[4], Susumu Shiomi[3] and Haruo Shintaku[1]

BACKGROUND: Congenital portosystemic shunt (CPSS) has the potential to cause hepatic encephalopathy and thus needs long-term follow-up, but an effective follow-up method has not yet been established. We aimed to evaluate the importance of per-rectal portal scintigraphy (PRPS) for long-term follow-up of CPSS.

METHODS: We retrospectively examined shunt severity time course in patients (median: 9.6 y, range: 5.2–16.6 y) with intrahepatic (n = 3) or extrahepatic (n = 3) CPSS by using blood tests, ultrasonography or computed tomography, and PRPS. Per-rectal portal shunt index (cutoff: 10%) was calculated by PRPS.

RESULTS: PRPS demonstrated that the initial shunt index was reduced in all intrahepatic cases (from 39.7±9.8% (mean ± SD) to 14.6±4.7%) and all extrahepatic cases (from 46.2±10.9 to 27.5±12.6%) during the follow-up period. However, ultrasonography and computed tomography disclosed different shunt diameter time courses between intrahepatic and extrahepatic CPSSs. Initial shunt diameter (5.8±3.5 mm) reduced to 2.0±0.3 mm in intrahepatic cases, but the initial diameter (6.3±0.7 mm) increased to 10.6±1.0 mm in extrahepatic cases. All patients had elevated serum total bile acid or ammonia levels at initial screening, but these blood parameters were insufficient to assess shunt severity because the values fluctuate.

CONCLUSION: PRPS can track changes in the shunt severity of CPSS and is more reliable than ultrasonography and computed tomography in patients with extrahepatic CPSS.

Congenital portosystemic shunt (CPSS), which is a major cause of neonatal hypergalactosemia without galactose-metabolizing-enzyme deficiency (1), causes brain manganese deposition, pulmonary hypertension, and hyperammonemia leading to hepatic encephalopathy (2–8). CPSS is generally suspected if serum total bile acid (TBA) and ammonia levels are elevated, and it is diagnosed by using color Doppler ultrasonography, dynamic contrast-enhanced computed tomography (CT), and per-rectal portal scintigraphy (PRPS) (7,9–12). Some shunts close spontaneously, whereas others need to be closed surgically or with embolization because of hyperammonemia leading to severe hepatic encephalopathy (7,8,13–15). Therefore, it is important to follow up CPSS patients carefully with color Doppler ultrasonography, dynamic contrast-enhanced CT, and blood tests. Despite this, there is no gold standard for accurately assessing the degree of shunt. Color Doppler ultrasonography and dynamic contrast-enhanced CT are useful for detecting shunt location and for assessing shunt diameter and flow, but these imaging modalities cannot be used to evaluate shunt severity quantitatively. By contrast, PRPS can be used to calculate a shunt index (SI) for quantifying shunt severity, as previously reported (9). Currently, the use of PRPS is limited to the diagnosis of CPSS, and its application to long-term follow-up of CPSS is uncertain. Here, we aimed to clarify the role for PRPS in the long-term follow-up of patients with CPSS by retrospectively evaluating changes in shunt severity over time as assessed with PRPS.

RESULTS

Patients

Six patients (mean age: 9.6 y; range: 5.2–16.6 y) were diagnosed as having CPSS during the first year of life. On the basis of ultrasonography and dynamic contrast-enhanced CT, three of the six patients were identified as having intrahepatic CPSS, and the remaining three patients were found to have extrahepatic CPSS (**Table 1**). None of the six patients had abnormalities in the abdominal cavity, including hepatic tumors. Two of the patients with intrahepatic CPSS had shunts between the left portal vein and the central hepatic vein, and one had a shunt between the left portal vein and left hepatic vein (**Table 1**). Of the patients with extrahepatic CPSS, two had splenorenal shunts (**Table 1**; **Figure 1a,b**), and one had a mesocaval shunt (**Table 1**; **Figure 1c**; **Supplementary Video S1** online). All six patients had normal mental development without hepatic encephalopathy and showed absence of pulmonary hypertension.

Shunt Diameter

Ultrasonography or dynamic contrast-enhanced CT, or both, disclosed a difference between intrahepatic and extrahepatic CPSSs in terms of changes in shunt diameter over time. All three

[1]Department of Pediatrics, Osaka City University Graduate School of Medicine, Osaka, Japan; [2]Department of Radiology, Osaka City University Graduate School of Medicine, Osaka, Japan; [3]Department of Nuclear Medicine, Osaka City University Graduate School of Medicine, Osaka, Japan; [4]Department of Genetics, Hyogo College of Medicine, Hyogo, Japan. Correspondence: Daisuke Tokuhara (m1155519@med.osaka-cu.ac.jp)

Received 20 July 2013; accepted 9 October 2013; advance online publication 12 March 2014. doi:10.1038/pr.2014.11

Table 1. Profiles of six children with congenital portosystemic shunt

Patient no.	Age at initial examination (mo)	Sex	Shunt location	Initial laboratory findings				
				Galactose[a] (<8 mg/dl)	TBA (<10 μmol/l)	NH_3 (30–80 μg/dl)	AST (20–70 IU/l)	ALT (10–70 IU/l)
1	0.5	Male	Intrahepatic (LPV–LHV)	14.97	37	178	23	18
2	1	Male	Intrahepatic (LPV–CHV)	8.9	44	89	41	28
3	1	Male	Intrahepatic (LPV–CHV)	11.6	56	141	30	19
4	1	Male	Extrahepatic (SV–LRV)	8.0	92.2	52	24	13
5	1	Male	Extrahepatic (SV–LRV)	8.0	184	94	55	40
6	1	Male	Extrahepatic (IMV–IIV)	7.4	58	80	38	23

ALT, alanine aminotransferase; AST, aspartate aminotransferase; CHV, central hepatic vein; IIV, internal iliac vein; IMV, inferior mesenteric vein; IU, international units; LHV, left hepatic vein; LPV, left portal vein; LRV, left renal vein; SV, splenic vein; TBA, total bile acid.
[a]Galactose was evaluated within 45 d after birth by newborn mass screening.

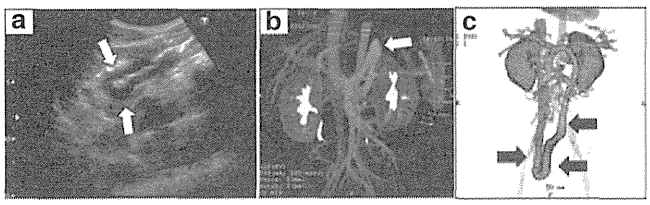

Figure 1. Ultrasonography and computed tomography (CT) portal venography of extrahepatic congenital portosystemic shunt patients. (**a**) Splenorenal shunt (arrow) was clearly visualized in the sagittal view on ultrasonography (16 y). (**b**) Splenorenal shunt (arrow) on maximum intensity projection image of CT portal venography (1.5 y). (**c**) Mesocaval shunt (arrow) on three-dimensional volume-rendered image of CT portal venography (5 y).

intrahepatic CPSS patients showed spontaneous shunt regression. The initial shunt diameter of 5.8 ± 3.5 mm (mean ± SD) at 0.7 ± 0.5 y of age was reduced to 2.0 ± 0.3 mm at 6 ± 2.6 y of age—a reduction of 59.6 ± 16.3% over 5.2 ± 2.8 y (Figure 2a–c). By contrast, the shunt diameter increased in all three extrahepatic CPSS patients: the initial shunt diameter of 6.3 ± 0.7 mm at 0.6 ± 0.2 y of age increased to 10.6 ± 1.0 mm at 11.3 ± 5.6 y of age—an increase of 70.0 ± 25.8% over 10.6 ± 5.6 y (Figure 2d–f).

Shunt Index

PRPS was performed in each patient two to four times at a median interval of 4.5 y (range: 1.4–6.7 y). For all six patients, the SI derived from PRPS decreased from 42.9 ± 9.9% (mean ± SD, cutoff: 10%) at 0.9 ± 0.8 y of age to 21.1 ± 11.1% at 9.3 ± 4.9 y of age (Figure 2; **Supplementary Figure S1** online)—a decrease of 51.8 ± 18.9% over 8.3 ± 5.2 y. In the patients with intrahepatic CPSS, the initial SI of 39.7 ± 9.8% at 1.2 ± 1.1 y of age decreased to 14.6 ± 4.7% at 6.6 ± 2.6 y of age (Figure 2a–c; **Supplementary Figure S1** online)—a reduction of 60.7 ± 19.9% over 5.4 ± 3.1 y. In the patients with extrahepatic CPSS, the initial SI of 46.2 ± 10.9% at 0.6 ± 0.4 y of age decreased to 27.5 ± 12.6% at 11.8 ± 5.6 y of age (Figure 2d–f; **Supplementary Figure S1** online)—a reduction of 42.9 ± 16.3% over 11.3 ± 5.7 y.

Blood Tests

Hypergalactosemia was identified in all six patients by newborn screening (Table 1). At the initial examination at our hospital, serum levels of TBA or ammonia were elevated in all six patients (Table 1). No elevations of aspartate aminotransferase and alanine aminotransferase levels were found in any of these patients. During the follow-up period, galactose levels decreased to within the normal range by 2 y of age despite persistent elevation of TBA and ammonia levels (Figure 3). The persistently high values of TBA or ammonia suggested the presence of a shunt, but the values fluctuated because of intestinal motility and changes in the types of meals consumed before fasting, limiting the use of these blood parameters in the quantitative assessment of shunt severity.

DISCUSSION

We retrospectively evaluated the long-term clinical course of CPSS patients, focusing on the degree of shunt as determined with PRPS. Various imaging modalities and blood tests indicated that the natural histories of intrahepatic and extrahepatic CPSSs differed. Intrahepatic CPSS without hepatic tumor has been reported to spontaneously close or regress, whereas extrahepatic CPSS does not spontaneously regress (3,7,8,16–18). Ultrasonography and dynamic contrast-enhanced CT evaluation showed spontaneous reductions in the shunt size in all of our patients with intrahepatic CPSS but in none with extrahepatic CPSS, strengthening the previous findings. Furthermore, all of our patients with extrahepatic CPSS showed marked enlargement in shunt diameter over time. The reason for this difference between intrahepatic and extrahepatic CPSSs is unclear; however, one possible explanation is the difference in the environments surrounding intrahepatic and extrahepatic CPSSs. An intrahepatic CPSS is tightly surrounded by liver parenchyma and may be under pressure during growth, perhaps leading to spontaneous closure. One case report of a child with intrahepatic CPSS who died of pulmonary hypertension described an enlarged portal tract with multiple thin-walled angiomatous vessels; these may be a feature of shunts that tend to close or regress under pressure (5). By contrast, an extrahepatic CPSS is under less pressure from the surrounding tissues and thus may retain its size, or enlarge, as the patient grows.

The most important finding of our study is the reduction in SI in extrahepatic CPSS, despite the increase in shunt diameter. PRPS is a noninvasive method that results in little exposure to

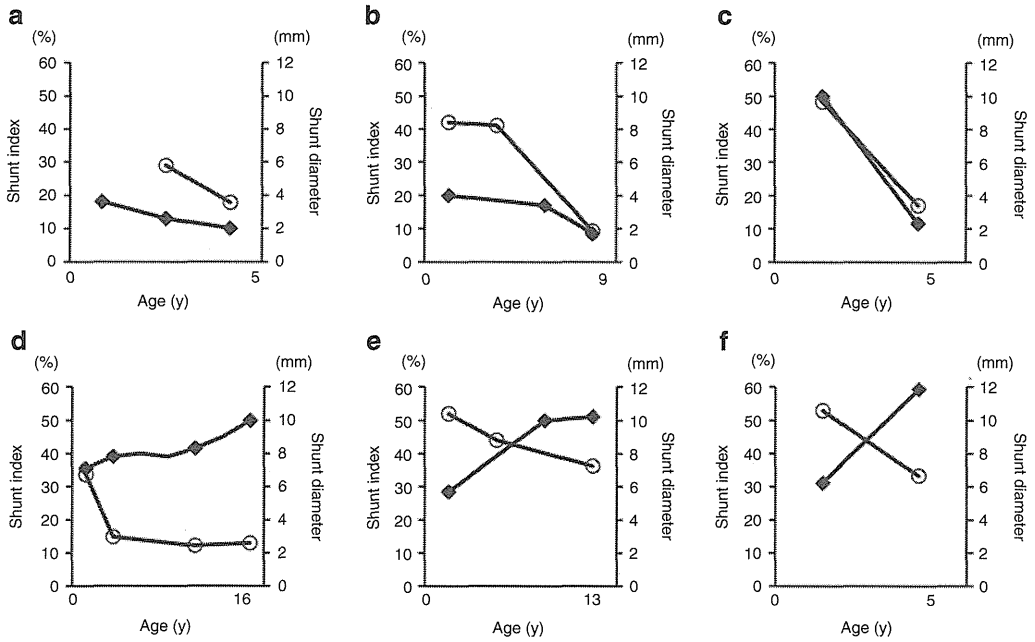

Figure 2. Time course of shunt index and shunt diameter in patients with congenital portosystemic shunt (CPSS). (**a**) Case 1 with intrahepatic CPSS between LPV and LHV. (**b**) Case 2 with intrahepatic CPSS between LPV and CHV. (**c**) Case 3 with intrahepatic CPSS between LPV and CHV. (**d**) Case 4 with extrahepatic CPSS between SV and LRV. (**e**) Case 5 with extrahepatic CPSS between SV and LRV. (**f**) Case 6 with extrahepatic CPSS between IMV and IIV. Case number is same as the patient number. Shunt index is shown as open circle, and shunt diameter is shown as solid diamond. CHV, central hepatic vein; IMV, inferior mesenteric vein; IIV, internal iliac vein; LHV, left hepatic vein; LPV, left portal vein; LRV, left renal vein; SV, splenic vein.

radionuclide and is an effective method for evaluating portal circulation; it is therefore used to diagnose or evaluate CPSS in children and to assess the severity of cirrhosis in adults (9,19–21). Shiomi *et al.* (19) reported the usefulness of PRPS in providing detailed information about changes in portal hemodynamics; they reported that SI in adults increases as liver cirrhosis progresses. Uchino *et al.* (3) reported that the risk of hepatic encephalopathy increases with the degree of portosystemic shunting, as indicated by the PRPS SI. The SI has also been shown to be useful for evaluating the postoperative course in dogs with extrahepatic CPSS (22). In children, a recent study demonstrated that PRPS is complementary to ultrasonography and endoscopy in the assessment of portal hypertension associated with chronic cholestasis (23). We found that SI decreased in all of our subjects with CPSS during long-term follow-up; this may be a previously unrecognized feature of the natural course of CPSS in humans. However, the change in SI paralleled a reduction in shunt diameter in the children with intrahepatic CPSS but contrasted with the increase in shunt diameter in patients with extrahepatic CPSS. CPSS without spontaneous closure or regression is considered to reflect an increase in the degree of shunt severity and is associated with complications (16). In addition, the enlargement of shunt diameter in our patients with extrahepatic CPSS may have led physicians to consider that the severity of the shunt has worsened. However, our study demonstrated that an increase in shunt diameter, as shown by imaging modalities such as ultrasonography and dynamic contrast-enhanced CT, is not an indicator of the severity of the shunt in CPSS, whereas PRPS can be used to quantify shunt severity by using the SI, regardless of changes in shunt appearance.

Imaging modalities such as ultrasonography and dynamic contrast-enhanced CT are useful for detecting the location and size of CPSS but cannot provide the degree of shunt severity as quantitatively as can PRPS. In addition, the image quality of ultrasonography for extrahepatic CPSS is often influenced by abdominal conditions (e.g., intestinal contents) because the shunt is surrounded by the stomach or the small or large intestine, whereas PRPS is not influenced by abdominal conditions because the radiological agent is instilled through the rectum. The concentrations of TBA and ammonia are useful for monitoring the presence of PSS, but because these values can fluctuate with changes in gut conditions, their use in accurately assessing progress toward shunt closure is problematic. Therefore, it is important and effective to use PRPS in addition to ultrasonography, dynamic contrast-enhanced CT, and blood tests to assess shunt severity in the diagnosis and follow-up of CPSS.

Surgical repair or embolization may be recommended for extrahepatic CPSS without closure because of the high risk of hepatopulmonary syndrome, pulmonary hypertension, and hepatic encephalopathy (4,7,8,13–16). Stringer (8) described that CPSS-affected individuals are at risk of developing hepatic encephalopathy and/or an intrahepatic tumor depending largely on the volume and duration of the shunt. The risk of hepatic encephalopathy is related to the degree of portosystemic shunting, as measured by PRPS (3); therefore, it is rational to take the SI into consideration when deciding whether surgical treatment or embolization is indicated. On the other hand, Bernard *et al.* (7) recommended that, even when no complication is detected, closure of shunt should be considered early to prevent complications

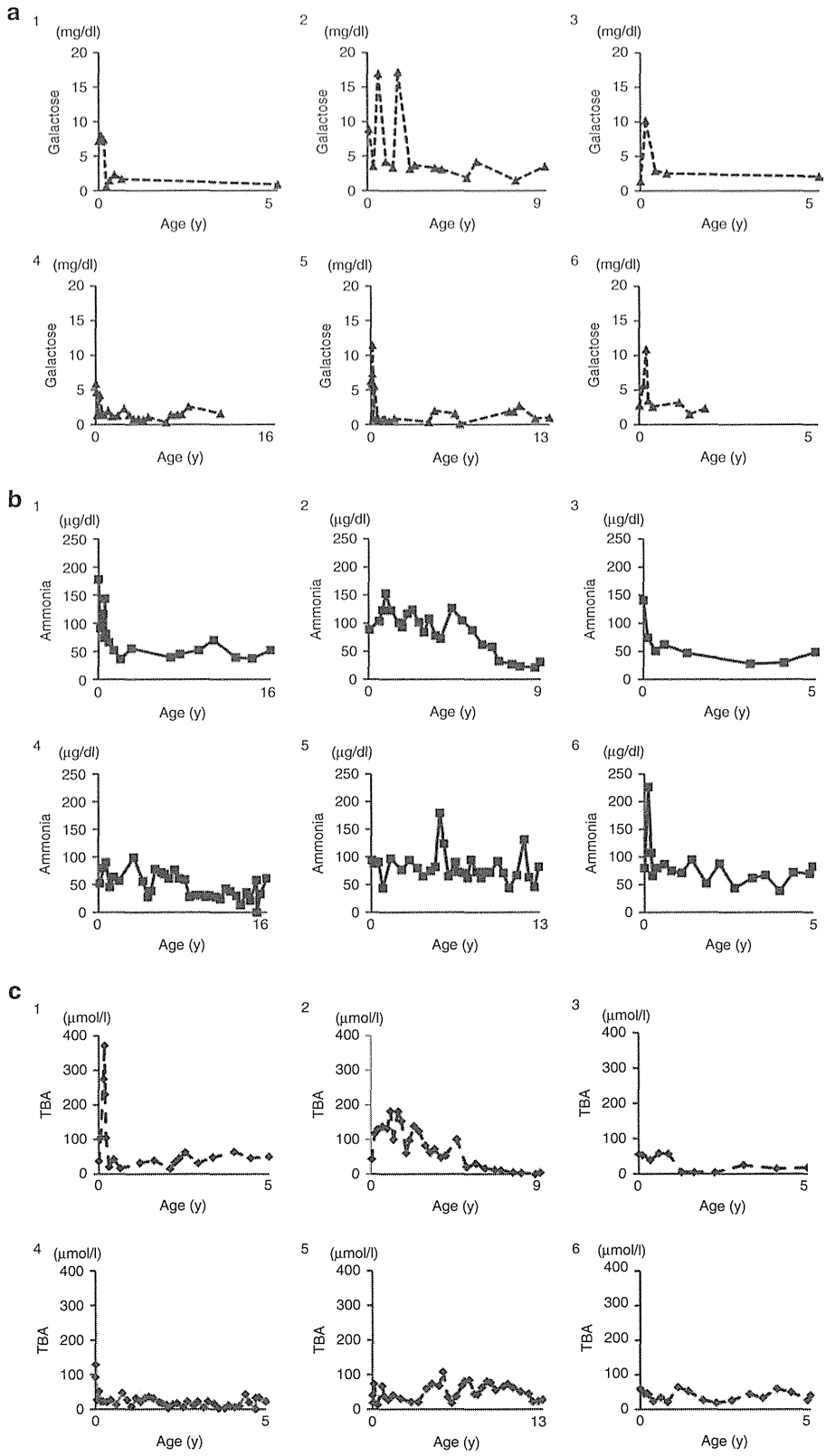

Figure 3. Time course of (**a**) galactose, (**b**) TBA, and (**c**) ammonia levels in children with congenital portosystemic shunt (CPSS). (1) Case 1 with intrahepatic CPSS between LPV and LHV. (2) Case 2 with intrahepatic CPSS between LPV and CHV. (3) Case 3 with intrahepatic CPSS between LPV and CHV. (4) Case 4 with extrahepatic CPSS between SV and LRV. (5) Case 5 with extrahepatic CPSS between SV and LRV. (6) Case 6 with extrahepatic CPSS between IMV and IIV. Case number is the same as patient number. CHV, central hepatic vein; IIV, internal iliac vein; IMV, inferior mesenteric vein; LHV, left hepatic vein; LPV, left portal vein; LRV, left renal vein; SV, splenic vein; TBA, total bile acid.

in cases of CPSS except for small intrahepatic shunt. Therefore, it remains unclear whether SI affects the indications for closure of shunt and there are no criteria for initiating treatment based on PRPS. In our study, the SI of extrahepatic CPSS decreased even though the shunt diameter increased during the long-term natural course of the condition. Taking the current and previous findings together suggests that it is important to determine the SI to evaluate the risk of hepatic encephalopathy in patients with extrahepatic CPSS; in addition, SI may be considered an important parameter in addition to hyperammonemia, portal pressure, shunt size, and clinical symptoms suggesting hepatic encephalopathy when deciding whether surgical treatment or embolization is warranted in patients with extrahepatic CPSS, although further clinical study is necessary to support this hypothesis.

In conclusion, our study clearly revealed that PRPS can provide information about the severity of CPSS beyond that provided by biochemical tests, ultrasonography, and dynamic contrast-enhanced CT. SI decreased over time, both in patients with intrahepatic CPSS, whose shunts decreased in diameter, and in patients with extrahepatic CPSS, whose shunts increased in diameter. We recommend following up patients with CPSS by using PRPS.

METHODS

Six patients with CPSS were retrospectively analyzed. Informed consent was obtained, and the study was approved by the Institutional Review Board of Osaka City University Hospital. All six patients were found to have hypergalactosemia during newborn screening but did not have galactose-metabolizing-enzyme deficiency. Each patient was diagnosed as having CPSS by blood tests, including aspartate aminotransferase, alanine aminotransferase, galactose, TBA, and ammonia levels, in addition to ultrasonography, dynamic contrast-enhanced CT, and PRPS. All patients were followed using the same modalities. Shunt location, shunt flow, and shunt diameter were evaluated by using ultrasonography and dynamic contrast-enhanced CT (Table 1). Chest roentgenography, electrocardiography, and echocardiography were undertaken to assess pulmonary hypertension. PRPS was performed as previously described (9). Briefly, a polyethylene tube (Nélaton's catheter, French 8–12, Terumo Cooperation, Tokyo, Japan) was inserted 10 cm deep into the rectum, reaching the upper part. A large-field scintillation camera (Vertex Plus; Adac Laboratories, Milpitas, CA) was used to generate time–activity curves. The camera had a low-energy, multipurpose, parallel-hole collimator and was interfaced with a digital computer (Pegasys; Adac Laboratories). The camera was positioned over the patient's abdomen so that the field of view included the heart, liver, and spleen. First, 111 MBq (megabecquerels) of Tc-99m–pertechnetate (1 ml) was given through the tube, followed by 10–20 ml of air. Thereafter, time–activity curves for the areas of the liver and heart were obtained every 4 s. At the end of the 5-min examination, the 5-min summed image, displayed in color, was recorded. To evaluate the extent of the portosystemic shunt in terms of an SI, we calculated the ratio of counts for the liver to counts for the heart integrated for 24 s immediately after the appearance of the liver time–activity curve.

SUPPLEMENTARY MATERIAL

Supplementary material is linked to the online version of the paper at http://www.nature.com/pr

REFERENCES

1. Nishimura Y, Tajima G, Dwi Bahagia A, et al. Differential diagnosis of neonatal mild hypergalactosaemia detected by mass screening: clinical significance of portal vein imaging. J Inherit Metab Dis 2004;27:11–8.
2. Mizoguchi N, Nishimura Y, Ono H, Sakura N. Manganese elevations in blood of children with congenital portosystemic shunts. Eur J Pediatr 2001;160:247–50.
3. Uchino T, Matsuda I, Endo F. The long-term prognosis of congenital portosystemic venous shunt. J Pediatr 1999;135(2 Pt 1):254–6.
4. Eroglu Y, Donaldson J, Sorensen LG, et al. Improved neurocognitive function after radiologic closure of congenital portosystemic shunts. J Pediatr Gastroenterol Nutr 2004;39:410–7.
5. Ersch J, Bänziger O, Braegger C, Arbenz U, Stallmach T. An infant with pulmonary hypertension due to a congenital porto-caval shunt. Eur J Pediatr 2002;161:660–2.
6. Ohno T, Muneuchi J, Ihara K, et al. Pulmonary hypertension in patients with congenital portosystemic venous shunt: a previously unrecognized association. Pediatrics 2008;121:e892–9.
7. Bernard O, Franchi-Abella S, Branchereau S, Pariente D, Gauthier F, Jacquemin E. Congenital portosystemic shunts in children: recognition, evaluation, and management. Semin Liver Dis 2012;32:273–87.
8. Stringer MD. The clinical anatomy of congenital portosystemic venous shunts. Clin Anat 2008;21:147–57.
9. Shiomi S, Sasaki N, Ikeoka N, et al. Usefulness of per-rectal portal scintigraphy with Tc-99m pertechnetate for galactosemia in infants. Ann Nucl Med 1998;12:375–8.
10. Kono T, Hiki T, Kuwashima S, Hashimoto T, Kaji Y. Hypergalactosemia in early infancy: diagnostic strategy with an emphasis on imaging. Pediatr Int 2009;51:276–82.
11. Mizoguchi N, Sakura N, Ono H, Naito K, Hamakawa M. Congenital porto-left renal venous shunt as a cause of galactosaemia. J Inherit Metab Dis 2001;24:72–8.
12. Sakura N, Mizoguchi N, Eguchi T, et al. Elevated plasma bile acids in hypergalactosaemic neonates: a diagnostic clue to portosystemic shunts. Eur J Pediatr 1997;156:716–8.
13. Yamagami T, Yoshimatsu R, Matsumoto T, et al. Successful embolization using interlocking detachable coils for a congenital extrahepatic portosystemic venous shunt in a child. J Pediatr Surg 2007;42:1949–52.
14. Ikeda S, Sera Y, Ohshiro H, Uchino S, Uchino T, Endo F. Surgical indications for patients with hyperammonemia. J Pediatr Surg 1999;34:1012–5.
15. Kimura T, Soh H, Hasegawa T, et al. Laparoscopic correction of congenital portosystemic shunt in children. Surg Laparosc Endosc Percutan Tech 2004;14:285–8.
16. Franchi-Abella S, Branchereau S, Lambert V, et al. Complications of congenital portosystemic shunts in children: therapeutic options and outcomes. J Pediatr Gastroenterol Nutr 2010;51:322–30.
17. Gitzelmann R, Forster I, Willi UV. Hypergalactosaemia in a newborn: self-limiting intrahepatic portosystemic venous shunt. Eur J Pediatr 1997;156:719–22.
18. Velayutham P, Dev A, Arora A. Congenital extrahepatic portocaval shunt: growth in vain. J Pediatr 2013;162:1076.e1.
19. Shiomi S, Kuroki T, Kurai O, et al. Portal circulation by technetium-99m pertechnetate per-rectal portal scintigraphy. J Nucl Med 1988;29:460–5.
20. Yoshimoto Y, Shimizu R, Saeki T, et al. Patent ductus venosus in children: a case report and review of the literature. J Pediatr Surg 2004;39:E1–5.
21. Kawamura E, Habu D, Hayashi T, et al. Natural history of major complications in hepatitis C virus-related cirrhosis evaluated by per-rectal portal scintigraphy. World J Gastroenterol 2005;11:3882–6.
22. Van Vechten BJ, Komtebedde J, Koblik PD. Use of transcolonic portal scintigraphy to monitor blood flow and progressive postoperative attenuation of partially ligated single extrahepatic portosystemic shunts in dogs. J Am Vet Med Assoc 1994;204:1770–4.
23. Vajro P, Celentano L, Manguso F, et al. Per-rectal portal scintigraphy is complementary to ultrasonography and endoscopy in the assessment of portal hypertension in children with chronic cholestasis. J Nucl Med 2004;45:1705–11.

RHEUMATOLOGY

Rheumatology 2014;53:448–458
doi:10.1093/rheumatology/ket372
Advance Access publication 3 December 2013

Original article

A nationwide survey of Aicardi–Goutières syndrome patients identifies a strong association between dominant *TREX1* mutations and chilblain lesions: Japanese cohort study

Junya Abe[1], Kazuyuki Nakamura[2], Ryuta Nishikomori[1], Mitsuhiro Kato[2], Noriko Mitsuiki[3,4], Kazushi Izawa[1], Tomonari Awaya[1], Tomoki Kawai[1], Takahiro Yasumi[1], Itaru Toyoshima[5], Kazuko Hasegawa[6], Yusei Ohshima[7], Toru Hiragi[8], Yoji Sasahara[9], Yasuhiro Suzuki[10], Masahiro Kikuchi[11], Hitoshi Osaka[12], Takashi Ohya[13], Shinya Ninomiya[14], Satoshi Fujikawa[15], Manami Akasaka[16], Naomi Iwata[17], Akiko Kawakita[7], Makoto Funatsuka[18], Haruo Shintaku[19], Osamu Ohara[3,20], Hiroshi Ichinose[21] and Toshio Heike[1]

Abstract

Objectives. Aicardi–Goutières syndrome (AGS) is a rare, genetically determined, early onset progressive encephalopathy associated with autoimmune manifestations. AGS is usually inherited in an autosomal recessive manner. The disease is rare, therefore the clinical manifestations and genotype–phenotype correlations, particularly with regard to autoimmune diseases, are still unclear. Here we performed a nationwide survey of AGS patients in Japan and analysed the genetic and clinical data.

Methods. Patients were recruited via questionnaires sent to paediatric or adult neurologists in Japanese hospitals and institutions. Genetic analysis was performed and clinical data were collected.

Results. Fourteen AGS patients were identified from 13 families; 10 harboured genetic mutations. Three patients harboured dominant-type *TREX1* mutations. These included two *de novo* cases: one caused by a novel heterozygous p.His195Tyr mutation and the other by a novel somatic mosaicism resulting in a p.Asp200Asn mutation. Chilblain lesions were observed in all patients harbouring dominant-type *TREX1* mutations. All three patients harbouring *SAMHD1* mutations were diagnosed with autoimmune diseases, two with SLE and one with SS. The latter is the first reported case.

Conclusion. This study is the first to report a nationwide AGS survey, which identified more patients with sporadic AGS carrying *de novo* dominant-type *TREX1* mutations than expected. There was a strong association between the dominant-type *TREX1* mutations and chilblain lesions, and between *SAMHD1* mutations and autoimmunity. These findings suggest that rheumatologists should pay attention to possible sporadic AGS cases presenting with neurological disorders and autoimmune manifestations.

Key words: Aicardi–Goutières syndrome, *TREX1*, *SAMHD1*, dominant-type, mosaicism, chilblain, autoimmunity.

[1]Department of Pediatrics, Kyoto University Graduate School of Medicine, Kyoto, [2]Department of Pediatrics, Yamagata University Faculty of Medicine, Yamagata, [3]Department of Human Genome Research, Kazusa DNA Research Institute, Kisarazu, [4]Department of Pediatrics and Developmental Biology, Graduate School of Medical and Dental Sciences, Tokyo Medical and Dental University, Tokyo, [5]Department of Neurology, National Hospital Organization Akita National Hospital, Yurihonjo, [6]Department of Neurology, National Hospital Organization, Sagamihara National Hospital, Sagamihara, [7]Department of Pediatrics, Faculty of Medical Sciences, University of Fukui, Fukui, [8]Department of Pediatrics, Tsuruga Municipal Hospital, Tsuruga, [9]Department of Pediatrics, Tohoku University Graduate School of Medicine, Sendai, [10]Department of Pediatric Neurology, Osaka Medical Center and Research Institute for Maternal and Child Health, Izumi, [11]Department of Pediatrics, Hitachi General Hospital, Hitachi, [12]Department of Neurology, Kanagawa Children's Medical Center, Yokohama, [13]Department of Pediatrics and Child Health, Kurume University School of Medicine, Kurume, [14]Department of Pediatrics, Nakatsu Municipal Hospital, Nakatsu, [15]Fujikawa Pediatrics Clinic, Tokyo, [16]Department of Pediatrics, Iwate Medical University School of Medicine, Morioka, [17]Department of Infection and Immunology, Aichi Children's Health and Medical Center, Obu, [18]Department of Pediatrics, Tokyo Women's Medical University, Tokyo, [19]Department of Pediatrics, Osaka City University Graduate School of Medicine, Osaka, [20]Laboratory for Immunogenomics, RIKEN Research Center for Allergy and Immunology, RIKEN Yokohama Institute, Yokohama and [21]Department of Life Science, Graduate School of Bioscience and Biotechnology, Tokyo Institute of Technology, Yokohama, Japan.

Submitted 22 July 2013; revised version accepted 24 September 2013.

Correspondence to: Ryuta Nishikomori, *Department of Pediatrics*, Kyoto University Graduate School of Medicine, 54 Kawahara-cho, Shogoin, Sakyo-ku, Kyoto 606-8507, Japan. E-mail: rnishiko@kuhp.kyoto-u.ac.jp

Introduction

Aicardi-Goutières syndrome (AGS) is a rare, genetically determined, early onset progressive encephalopathy [1]. Patients with AGS typically suffer from irritability, inconsolable crying and progressive microcephaly associated with severe neurological symptoms, such as hypotonia, dystonia, seizures, spastic quadriplegia and severe developmental delay [2]. On brain imaging, AGS is characterized by calcifications of basal ganglia, white matter abnormalities and cerebral atrophy [3, 4]. Cerebrospinal fluid (CSF) analysis shows chronic lymphocytosis and elevated IFN-α and neopterin levels [3–5]. AGS patients are often misdiagnosed as having intrauterine infections, such as TORCH (toxoplasmosis, other infections, rubella, cytomegalovirus infection and herpes simplex) syndrome, because of the similarities in the clinical findings, particularly the intracranial calcifications [1]. As extraneural findings, chilblain lesions are seen in approximately 40% of patients [3]. Some patients also show bouts of mild fever, hepatosplenomegaly, abnormal liver function and thrombocytopenia [1, 3, 4].

Mutations in five genes—*TREX1*, *RNASEH2B*, *RNASEH2C*, *RNASEH2A* and *SAMHD1*—are linked with AGS [6–8]. Approximately 90% of patients with characteristic clinical and radiologic findings of AGS harbour aetiological mutations in one of these five genes [1]. The *ADAR1* gene was recently identified as a sixth gene linked with AGS [9]. AGS is often inherited in an autosomal recessive manner, although a few cases show an autosomal dominant pattern of inheritance [2, 10–12]. Mutations in *TREX1* are often associated with early onset neonatal AGS, which presents with more severe neurological features, whereas *RNASEH2B* mutations are related to a later-onset presentation that is associated with less severe neurological problems and lower mortality rates [2, 3].

The main pathophysiological feature of AGS is the overproduction of type I IFN, caused by the accumulation of nucleic acids within cells stimulating the pattern recognition receptors and the innate immune system [1]. Therefore AGS can be regarded as an interferonopathy [13]. SLE is also an interferonopathy and shares many clinical features with AGS, including skin lesions, neurological abnormalities and the expression of type I IFN-related genes [13, 14]. Some SLE patients harbour *TREX1* mutations, suggesting that AGS and SLE are both allelic disorders that share a common pathophysiology, overproduction of type I IFN [15]. AGS is a disease of monogenic autoimmunity and an important disorder that must be considered when making a differential diagnosis of SLE; indeed, some molecularly proven AGS patients fulfil the diagnostic criteria for SLE [2, 16, 17]. In addition, AGS is similar, particularly with regard to skin lesions, to familial chilblain lupus (FCL), a rare cutaneous form of SLE that shows Mendelian inheritance [18]. We recently reported a family containing AGS and FCL cases caused by a heterozygous p.Asp18Asn mutation in *TREX1*, and proved the clinical continuity of these two conditions [19]. Although the similarities between SLE and AGS are known, the autoimmune aspects of AGS are still unclear because of the rarity of the disorder.

As a rare monogenic disorder, AGS reports have predominantly examined individual AGS families. Alternatively, some genetic analysis centres have recruited AGS patients from around the world. Here we report the first nationwide survey of Japanese AGS patients, which was conducted using questionnaires designed to identify the clinical manifestations and genotype–phenotype correlations in detail, with a particular focus on autoimmune symptoms.

Materials and methods

Patients

Questionnaires were sent to 1852 hospitals and institutions that specialize in paediatric and adult neurology, and 760 replies (41.0%) were received. Detailed questionnaires were then sent to the hospitals or institutions with positive replies and clinical information regarding suspected AGS cases was obtained. In addition, some patients enrolled in the study were referred directly to our institution by paediatric neurologists and paediatric rheumatologists. Clinical information, patient histories and laboratory data were collected from medical records and by direct interviews with patients, their families and their attending physicians. Neuroimaging data included CT scans and/or MRI scans. AGS was diagnosed according to the following criteria: (i) neurological abnormalities of encephalopathy, (ii) intracranial calcifications, (iii) the absence of prenatal infection and (iv) at least one CSF abnormality, such as a white cell count $\geqslant 5$ cells/mm^3, elevated IFN-α levels (>6 IU/ml or >12.5 pg/ml), or raised neopterin levels (reference ranges 8.0–25.0 nM at an age of 2–12 years and 7.3–31.6 nM in adults). In cases with no available CSF data, a diagnosis of AGS was made when the patients fulfilled criteria 1–3 and either had mutations in the genes responsible for AGS or had siblings who had been diagnosed with AGS.

Laboratory data

IFN-α levels were measured using a cytopathic effect inhibition assay (SRL, Tokyo, Japan). In the present study, a value >6 IU/ml was considered elevated due to the limit of detection of the assay, although most previous reports considered >2 IU/ml as the cut-off value for AGS. In some cases, IFN-α was measured by ELISA (SRL). The CSF neopterin level was measured as previously described [20].

Genetic analysis

The nationwide survey was approved by the ethical committee of the National Hospital Organization, Sagamihara National Hospital, and genetic analyses were approved by the ethical committees of Kyoto University Hospital and the National Hospital Organization, Sagamihara National Hospital, in accordance with the Declaration of Helsinki. After obtaining written informed consent from all study subjects (or their parents or guardians), genetic analyses

of *TREX1*, *RNASEH2B*, *RNASEH2C*, *RNASEH2A* and *SAMHD1* were performed. Genetic analysis of the *ADAR1* gene was performed for those patients clinically diagnosed with AGS but who did not harbour a mutation in any of these genes. Genomic DNA was extracted from the whole blood samples taken from the patients and their parents (if available) and all exons, including the exon–intron boundaries, were sequenced as previously described [21]. *TREX1* gene mosaicism was analysed using massively parallel DNA sequencing as previously described [22]. Leucocyte subpopulations were isolated and sorted using an autoMACS Pro Separator (Miltenyi Biotec, Gladbach, Germany) as previously described [23]. The purity of the isolated subpopulations was >90%.

Exonuclease assays

The pFN18A HaloTag T7 Flexi Vector system (Promega, Madison, WI, USA) with a HaloTag at the N-terminus was used to generate a recombinant human TREX1 protein. Recombinant protein was produced in Single Step (KRX) Competent Cells (Promega) and isolated according to the manufacturer's protocol. The recombinant proteins were then immunoblotted with an anti-TREX1 antibody (Sigma-Aldrich, St Louis, MO, USA) as previously described [21]. The concentrations of the purified TREX1 proteins were determined using the Flamingo Fluorescent Gel Stain (Bio-Rad, Hercules, CA, USA) assay with a Molecular Imager FX Pro Plus (Bio-Rad).

The ssDNA and dsDNA exonuclease assays were performed according to the method of Orebaugh *et al.* [24]. Briefly, for the ssDNA assays, a 30-mer oligonucleotide with 5′-fluorescein (6-FAM) (Sigma-Aldrich) and TREX1 proteins were incubated at 37°C for 30 min, followed by separation on 23% denaturing polyacrylamide gels. Using the visualized fluorescein-labelled bands, the fraction of oligomer at each position was multiplied by the number of excised deoxynucleoside monophosphates (dNMPs) to determine the activities of the recombinant TREX1 proteins (fmol of dNMP/s/fmol of enzyme). For the dsDNA assays, the p3xFLAG CMV-14 plasmid (Sigma-Aldrich), which contains a single Nt.BbvCI site (New England Biolabs, Ipswich, MA, USA), was digested by Nt.BbvCI. The nicked plasmid DNA was then incubated with the TREX1 proteins at 25°C for 30 min, followed by separation in electrophoresis on 0.8% agarose gels. Using SYBR Green I (Lonza, Basel, Switzerland), the excised dNMPs and activities of the recombinant TREX1 proteins (fmol of dNMP/s/fmol of enzyme) were calculated by the amount of degraded dsDNA.

Statistical analysis

Fisher's exact test was used to examine differences in categorical variables among the cohort in the present study or between the cohort in the present study and cohorts from other studies. Statistical significance was set at $P < 0.05$.

Results

Genetic and molecular findings

We identified 14 AGS patients from 13 families. All patients were Japanese and none were consanguineous. Of the 13 families, 10 harboured mutations and 3 did not (Table 1). Altogether, we identified 15 mutations in four genes, 10 of which were novel. All of the novel mutations were absent from at least 100 Japanese control alleles and from the 1000 Genomes Project database. Six of the novel mutations were missense mutations. PolyPhen-2 analysis predicted five to be probably damaging and the other, a p.Gly258Val mutation in *SAMHD1*, to be possibly damaging; all were predicted to be deleterious by sorting intolerant from tolerant (SIFT) analysis. The median age of the patients at the time of genetic analysis was 6 years (range 6 months–18 years).

Of the 10 families harbouring mutations, 5 harboured mutations in *TREX1*, 3 in *SAMHD1*, 1 in *RNASEH2B* and 1 in *RNASEH2A*. None of the families harboured mutations in *RNASEH2C* or *ADAR1*. No families harboured homozygous mutations. The *RNASEH2B* mutation was heterozygous; however, the mother who showed no symptoms of AGS shared the same heterozygous

TABLE 1 Genetic findings of Aicardi–Goutières syndrome patients

Patient	Gene	Nucleotide change	Protein change
1	AGS1/*TREX1*	c.[52G>A];[=]	p.[Asp18Asn];[=]
2	AGS1/*TREX1*	c.[**583C>T**];[=], *de novo*	p.[**His195Tyr**];[=], *de novo*
3	AGS1/*TREX1*	c.[=/598G>A], *de novo*	p.[=/Asp200Asn], *de novo*
4	AGS1/*TREX1*	c.[**667G>A**];[**839delG**]	p.[**Ala223Thr**];[**Gly280Glufs*18**]
5	AGS1/*TREX1*	c.[**839delG**];[859_876del18]	p.[**Gly280Glufs*18**];[Leu287_Gly292del]
6	AGS2/*RNASEH2B*	c.[**155T>G**];[=]	p.[**Leu52Trp**];[=]
7	AGS4/*RNASEH2A*	c.[**557G>A**];[**703C>T**]	p.[**Arg186Gln**];[**Arg235Trp**]
8	AGS5/*SAMHD1*	c.[368A>C];[**1567A>T**]	p.[His123Pro];[**Lys523***]
9	AGS5/*SAMHD1*	c.[**773G>T**];[**1141_1143delATT**]	p.[**Gly258Val**];[**Ile381del**]
10	AGS5/*SAMHD1*	c.[428G>A(;)**1435G>T**]	p.[Arg143His(;)**Glu479***]

Novel mutations are indicated in bold. Consanguinity was not present in any of the families of these AGS patients. = denotes normal sequence, and * denotes nonsense variant.

mutation and further analyses were not performed due to a lack of additional samples of the patient or the family.

Three families (patients 1–3) harboured *TREX1* mutations on one allele only. The patient harbouring the heterozygous p.Asp18Asn mutation (patient 1) had a maternal family history of FCL, which was caused by the same mutation [19]. Parental genotyping showed that the other two mutations, p.His195Tyr and p.Asp200Asn (patients 2 and 3), were *de novo* (Fig. 1A and B). RT-PCR analyses also confirmed a lack of additional mutations in *TREX1* of the three patients.

Since dominant-type *TREX1* mutations are a very rare cause of AGS [2, 10–12], we performed additional biochemical analyses of the three dominant mutations identified in our cohort, particularly the novel p.His195Tyr mutation (patient 2), to confirm their mutational effects. The TREX1 protein contains three exonuclease domains that form the active site of the enzyme, and His195, located in the third exonuclease domain, is the catalytically important histidine (Fig. 1C) [25–28]. First, we confirmed that His195 was highly conserved among different species (Fig. 1D). Next, we generated recombinant human TREX1 proteins (Fig. 1E) and compared them with wild-type TREX1 proteins ($TREX1^{WT}$). The ssDNA and dsDNA exonuclease assays revealed that TREX1 proteins harbouring the p.His195Tyr mutation ($TREX1^{p.His195Tyr}$) showed a marked reduction in enzymatic activity, similar to TREX1 proteins harbouring the p.Asp18Asn ($TREX1^{p.Asp18Asn}$) and p.Asp200Asn ($TREX1^{p.Asp200Asn}$) mutations, which are reported to cause dominant-type AGS (Fig. 1F and G) [10, 11].

In addition, we identified a patient harbouring *TREX1* with a p.Asp200Asn mutation (patient 3), in which the signal intensity of the mutated A at position 598 was lower than that of the reference G (Fig. 1B). Since this result suggested that a somatic mosaicism can cause AGS, we performed additional genetic analyses. Massively parallel DNA sequencing showed that neutrophils, monocytes, T cells, B cells and cells of the buccal mucosa harboured the same mutation at frequencies of approximately 20–30%, suggesting that the mutation occurred at an early stage of development and that approximately half of the mutated and normal cells co-existed in the patient.

FIG. 1 Genetic and molecular analyses of the *TREX1* mutations

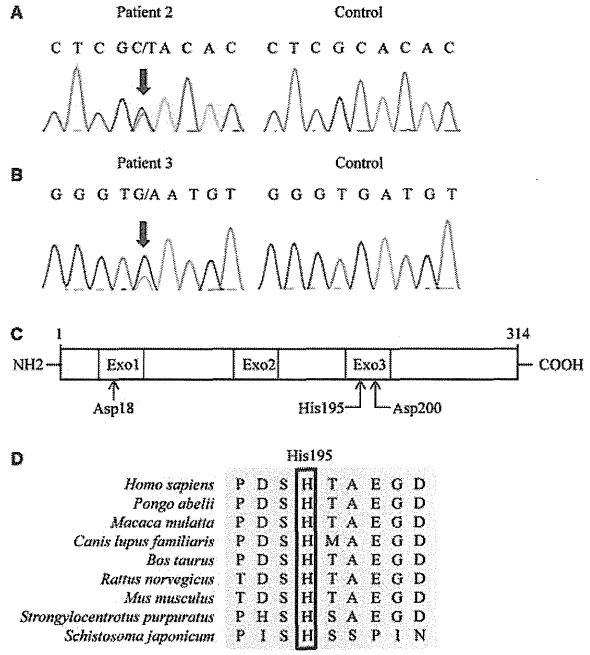

(**A**) Chromatograms for the direct sequencing of the *TREX1* gene from patient 2 and from a healthy control. The arrow indicates the heterozygous c.583C>T substitution, which leads to the p.His195Tyr mutation. (**B**) Chromatograms for the direct sequencing of the *TREX1* gene from patient 3 and from a healthy control. The arrow indicates the mutant A allele: the signal intensity of this mutation, at position 598, is lower than that of the reference G, suggesting somatic mosaicism of c.598G>A, which leads to the p.Asp200Asn mutation. (**C**) Schematic representation of the human TREX1 protein. Exo1–3 shows the three exonuclease domains that form the active site. The arrows indicate the positions of Asp18, His195 and Asp200. Mutations in these amino acid residues can cause dominantly inherited AGS. (**D**) Alignment of the TREX1 protein sequences. His195 is highly conserved from *Schistosoma japonicum* to *Homo sapiens*.

Clinical findings

All of the patients in the present cohort are currently alive (Table 2). Of the 13 patients for whom neonatal information was available, 11 were born at term, but 6 were small for their gestational age. All patients showed the first symptoms of AGS within 6 months of birth, with a median disease onset of 1.5 months. Four patients (patients 9, 11, 13 and 14) were early onset cases, which were affected within the first days of life; patients 9 and 11 had thrombocytopenia at the time of disease onset. Of the other subacute-onset cases, the earliest symptoms were largely related to encephalopathy, including neurological abnormalities and fever; however, patients 1 and 2 presented with rashes on the extremities that were later diagnosed as chilblains.

In the present study, all patients showed developmental delay, which was severe in 13 cases and moderate in 1 (patient 1). Seizures were observed in seven patients (patients 1, 5, 7, 8, 11, 13 and 14), including febrile convulsions in two. We also identified microcephaly in nine patients (patients 4–10, 12 and 14), dystonia in six (patients 5, 6, 8, 9, 12 and 13) and hypotonia in five (patients 2, 5, 7, 9 and 13).

Chilblain lesions were observed in seven patients (patients 1–5, 8 and 10) (Fig. 2A). All five patients harbouring *TREX1* mutations had chilblain lesions, which were absent in patients without gene mutations. The lesions

FIG. 2 Genetic and molecular analysis of the *TREX1* mutations

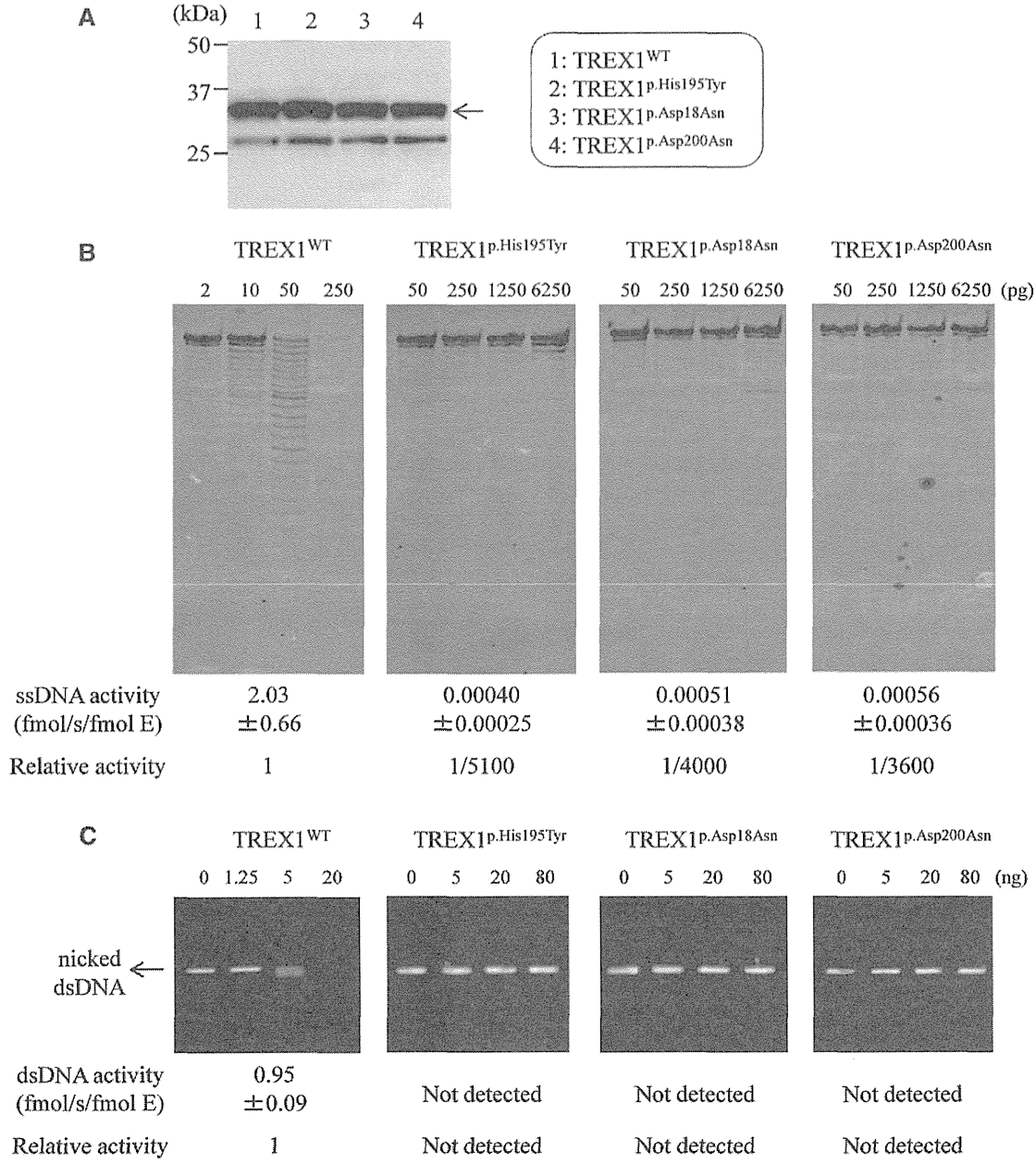

(**A**) Western blotting of purified recombinant human TREX1 proteins expressed in bacteria. The arrow indicates the position of the TREX1 proteins. The exonuclease activity of the recombinant TREX1 proteins in the (**B**) ssDNA assay and the (**C**) dsDNA assay. The amount of TREX1 protein used in the assays is indicated. The enzymatic activity of wild-type and mutated TREX1 proteins and the relative activity, which is shown as the ratio of the activity of the mutant to that of the wild type, are shown below each figure. Values are expressed as the mean (S.D.) of three independent experiments. The arrow in (C) indicates non-degraded, nicked dsDNA.

appeared on the fingers and toes in all seven cases; four of the seven also had lesions on the ears. In all cases the lesions were worse during the winter.

Recurrent fever was observed in seven patients (patients 1, 2, 4, 5, 8, 9 and 13). Regarding articular diseases, patient 4 suffered from scoliosis and a hip dislocation, and patient 10 had arthritis. Patients 7 and 9 suffered from hearing loss, and four patients (patients 2, 4, 8 and 14) had ophthalmological problems.

Patients 8 and 9, both harbouring *SAMHD1* mutations, fulfilled the ACR diagnostic criteria for SLE [29]. In addition, patient 10, who also harboured a *SAMHD1* mutation, was diagnosed with SS according to the Japanese criteria for SS [30].

Table 2 Clinical findings of Aicardi-Goutières syndrome patients

Patient	Genotype	Age, years	Sex	GA, weeks	BW, g	Age at disease onset	Manifestations at disease onset	Developmental delay	Other neurological manifestations	Chilblain lesions	Extraneural manifestations
1	*TREX1* AD	15	F	38	2840	23 d	Rash (extremities)	Moderate	Febrile convulsion	Yes	Recurrent fever, abdominal pain
2	*TREX1* AD	15	M	39	2792	2 mo	Rash (extremities)	Severe	Hypotonia	Yes	Recurrent fever, conjunctivitis, posterior synechia
3	*TREX1* AD	8	M	39	2828	4 mo	Delayed head control	Severe	None	Yes	None
4	*TREX1* AR	19	F	38	2044	3 mo	Delayed head control	Severe	Microcephaly, spastic quadriplegia	Yes	Recurrent fever, oral ulcer, abdominal pain, visual impairment, scoliosis, hip dislocation, neurogenic bladder dysfunction
5	*TREX1* AR	12	M	38	3000	18 d	Fever	Severe	Dystonia, hypotonia, microcephaly, febrile convulsion, mixed quadriplegia, startle reaction	Yes	Recurrent fever
6	*RNASEH2B* ?	6	F	Unknown	Unknown	3 mo	Eye movement disorder	Severe	Dystonia, microcephaly	No	None
7	*RNASEH2A* AR	2	F	36	1931	3 mo	Involuntary movement	Severe	Hypotonia (trunk), hypertonia (extremities), microcephaly, seizure	No	Hearing loss
8	*SAMHD1* AR	14	F	40	2052	1 mo	Irritability	Severe	Dystonia, microcephaly, seizure	Yes	Recurrent fever, hepatosplenomegaly, glaucoma, corneal perforation
9	*SAMHD1* AR	6	F	38	2534	5 d	Fever and feeding difficulties with thrombocytopenia	Severe	Dystonia, hypotonia, microcephaly	No	Recurrent fever, photosensitization, hearing loss
10	*SAMHD1* AR	16	M	39	2330	<4 mo	Irritability	Severe	Microcephaly	Yes	Arthritis
11	ND	4	M	36	2780	4 d	Omphalitis with thrombocytopenia	Severe	Hypertonia, seizure, spastic quadriplegia	No	Idiopathic interstitial pneumonia
12	ND	6	M	39	3290	6 mo	Developmental delay	Severe	Regression, dystonia, microcephaly	No	Atopic dermatitis
13	ND	7	F	40	2144	0 d	Conjugate deviation	Severe	Dystonia, hypotonia, seizure, spastic paralysis	No	Recurrent fever
14	ND	4	F	37	2056	0 d	Conjugate deviation	Severe	Regression, microcephaly, seizure, hemiplegia	No	Congenital cataract

GA: gestational age; BW: birth weight; AR: autosomal recessive; AD: autosomal dominant; ND: not detected; M: male; F: female; d: day(s); mo: month(s). Patients 1–10 are the same as presented in Table 1. No significant mutations in six genes associated with AGS were detected in patients 11–14. Patients 13 and 14 are siblings.